Thesis for the degree of Licentiate of Philosophy

Microscopic Modeling of Exciton-Polaritons in Two-Dimensional Materials

Beatriz Ferreira

Department of Physics

Chalmers University of Technology

Göteborg, Sweden 2022

Microscopic Modeling of Exciton-Polaritons in Two-Dimensional Materials
Beatriz Ferreira

Department of Physics
Chalmers University of Technology
SE-412 96 Göteborg
Sweden
Telephone + 46 (0)31-772 1000

Cover illustration: Schematic illustration of a TMD (transition metal dichalcogenide) monolayer in a Fabry-Perot cavity with the fundamental cavity mode represented by the red curve. TMD excitons-polaritons interact with photons and phonons as indicated by the yellow and orange arrows.

Printed at Chalmers Reproservice
Göteborg, Sweden 2022

Microscopic Modeling of Exciton-Polaritons in Two-Dimensional Materials
Beatriz Ferreira
Department of Physics
Chalmers University of Technology

Abstract

Integrating 2D materials into high-quality optical microcavities opens the door to fascinating many-particle phenomena including the formation of exciton-polaritons. These are hybrid quasi-particles inheriting properties of both the constituent photons and excitons. The corresponding change in the dispersion relation has a large impact on the optics, dynamics and transport behaviour of the materials.
In this thesis, we aim to microscopically understand the optical response and propagation of exciton-polaritons in transition metal dichalcogenides (TMDs). The theoretical method is based on the density matrix formalism combined with the Hopfield approach. In particular, we investigate how the diffusion of exciton changes in the strong coupling regime, i.e. when exciton-polaritons are formed. Furthermore, we study the impact of dark excitons on the optical response of upper and lower polariton branches in absorption spectra of molybdenum- and tungsten-based TMDs, which are known to be direct and indirect semiconductors, respectively. Furthermore, we show how different experimentally accessible quantities, such as temperature or mirror reflectance, can be exploited to tune the optical response of polaritons. Our study contributes to an improved microscopic understanding of exciton-polaritons and their interaction with phonons, potentially suggesting experiments that could determine the energy of dark exciton states via momentum-resolved polariton absorption.

Keywords: exciton-polaritons, 2D materials, diffusion, absorption.

List of publications

This thesis consists of an introductory text and the following published articles:

I. **Microscopic modeling of exciton-polariton diffusion coefficients in atomically thin semiconductors**
Beatriz Ferreira, Roberto Rosati, and Ermin Malic
Physical Review Materials **6**, 034008 (2022)

II. **Signatures of dark excitons in exciton-polariton optics of transition metal dichalcogenides**
Beatriz Ferreira, Roberto Rosati, Jamie M. Fitzgerald, and Ermin Malic
2D Materials **10**, 015012 (2023)

Publications not appended in this thesis:

III. **Tuning of the polariton absorption in WSe_2 and $MoSe_2$ monolayers**
Beatriz Ferreira, Roberto Rosati, Jamie M Fitzgerald, and Ermin Malic
In preparation

My contribution to the listed publications
As the first author of Paper I, I developed the theoretical model, performed the numerical evaluations, analyzed the results and wrote the manuscripts with the aid of my main supervisor and the other authors. In Papers II-III, I performed the numerical evaluations, analyzed the results and wrote the manuscripts with the aid of my main supervisor and the other authors.

Contents

CHAPTER 1

Introduction

Excitons have been the object of study in several areas of research and different materials [1, 2]. They are a bound pair of an electron and a hole, due to the electron being excited from the valence to the conduction band in a semiconductor material. The easiest way to excite excitons is by optical excitation [3]. However, the coupling to light strongly influences the physical properties and energy spectrum of these particles [4]. So in the late 50s, in the works of Agranovic [5] and Hopfield [6], the term *polariton* appeared to describe the coupling of exciton-photons. However, the word polariton is not exclusive to exciton-polaritons. Polaritons are hybrid states due to the interaction between light and matter, between an elementary matter excitation and a photon [7]. So, depending on the nature of this matter excitation we have different types of polaritons, like the surface plasmon-polaritons [8], phonon-polaritons [9], magnon-polaritons [10], among others. To be more specific, the polariton is a coupled mode of the external electromagnetic field with an electric or magnetic dipole-carrying excitation, meaning a normal mode of the material which may couple in a linear manner to the electromagnetic field by virtue of their electrical or magnetic character [7]. This external

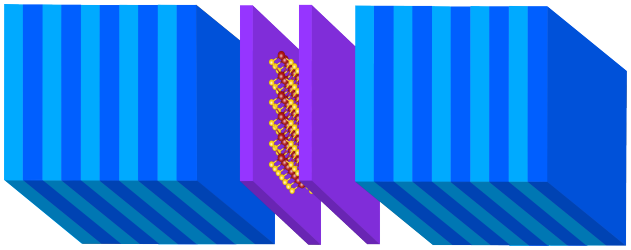

Figure 1.1: Schematic illustration of an hBN-encapsulated TMD monolayer in a Fabry-Perot cavity.

electromagnetic field can couple to single particle electronic excitations, as interband transitions in insulators, or to collective electronic excitations, as excitons. The exciton-polaritons are quasi-particles that maintain characteristics of both photons and excitons, such as a small effective mass, which makes them attractive for transport purposes [11–13].
Polaritons have been extensively studied in bulk semiconductor materials [14, 15], thin films [16, 17], quantum wells [18, 19], etc. Exciton–polaritons in microcavities have very particular properties resulting from the reduced dimensionality compared to other systems with no optical confinement [4, 20]. In particular, the strength of exciton–light coupling is greatly enhanced in microcavities and is larger than (the difference of) cavity and non-radiative exciton decay rates [21]. This results in the so-called strong-coupling regime manifested by the anticrossing of the exciton-polariton modes [22]. This allows the formation of polaritons as true new eigenmodes of the system, which appeared to be split at the anticrossing point [6]. The energy difference between modes at this point is widely referred to as vacuum-field Rabi splitting or simply Rabi splitting.

Exciton-polaritons were studied primarily on semiconductor quantum-well systems, where many groundbreaking discoveries were made such as Bose-Einstein condensation, polariton lasing and superfluidity [22–26]. Despite all these outstanding achievements in fundamental science, applications based on quantum-well systems were limited by their relatively small exciton binding energy, typically below room temperature thermal energy ($\approx$ 26 meV). However, with the discovery of 2D materials, a new interest in this area reappeared. Particularly, with the integration of transition metal dichalcogenides (TMDs) into optical cavities [27–29] (see schematic Fig.1.1), since

polaritons in these materials show room-temperature stability, long-distance propagation, and controllability through electric gating, valley-selective optical pumping, and precise thickness control. Consequently, this allowed, once again, the study of intriguing effects, such as Bose-Einstein condensation [30–32], (super)fluidity [33, 34], topological effects [35], and promising applications from lasing [36], to integrated circuits [37] and quantum computing [38].

Previous studies have shown that TMD monolayers with their rich exciton landscape, including dark and bright exciton states [39–41], exhibit interesting spatio-temporal exciton dynamics resulting in an intriguing exciton diffusion behaviour [2]. This includes non-classical diffusion [42], transient negative diffusion [43], strain-dependent (increase of) diffusion [44], accelerated hot-exciton diffusion [45] or formation of spatial rings (halos) [46–48] and unconventional exciton funnelling effects [49]. However, heterostructures of TMDs, both vertical and lateral, have very interesting properties too, like interlayer or charge transfer excitons [50–61]. Once embedded in a cavity, this gives rise to peculiar polaritonic effects [2, 62]. In view of their light component, polaritons show an interesting transport behaviour resulting in a fast propagation in the ballistic regime [11, 13]. The polariton diffusion has already been observed e.g. in ZnSe and GaAs films [63, 64]. In this thesis, we microscopically study the polaritonic diffusion coefficients. We combine the exciton density matrix formalism [65, 66] with the Hopfield approach [6, 21], where the exciton energies and wavefunctions in TMD monolayers are obtained by solving the Wannier equation [67–69] including DFT input on the characteristics of the electronic bandstructure [70]. We focus on an hBN-encapsulated $MoSe_2$ monolayer, which we find to be a direct semiconductor with the bright KK excitons (electron and hole located at the K point) as energetically lowest states [40]. In contrast, tungsten-based TMDs are known to be indirect semiconductors with momentum-dark excitons as energetically lowest states [40, 41, 71]. Since light-matter coupling is not directly affected, we expect smaller polariton-induced changes in the diffusion coefficient for tungsten-based materials. We investigate the change in the group velocity and polariton-phonon scattering rates as crucial ingredients determining the diffusion coefficient. Based on our microscopic approach, we predict a polariton diffusion coefficient up to three orders of magnitude higher compared to bare exciton diffusion.

In the context of optoelectronics, the huge light-matter interaction demonstrated by TMDs has made them highly attractive for practical device applications [27]. Liu *et al* were the first to confirm the formation of polariton states in a MoS_2 monolayer integrated into a microcavity by performing angle-resolved reflectivity and photoluminescence measurements. The signature of dark excitons can be found in the optical spectrum of TMDs [39]. So, we study the polariton absorption for hBN-encapsulated TMDs monolayers, WSe_2 and $MoSe_2$. By comparing a direct and indirect TMD, we can determine the impact of the dark excitons. Also, the polariton absorption is especially informative as it unambiguously demonstrates strong coupling via the Rabi splitting [4], and its magnitude is determined by the balance between the polariton-phonon and cavity decay rates. Hence, besides the previous theoretical framework used in diffusion, we also add the Heisenberg-Langevin equations together with the input-output formalism [72]. This time, we calculate the full valley- and momentum-dependent polariton-phonon scattering rates that govern the optical response of TMD materials via both spectral linewidths and magnitude. Our results found that dark excitons are significantly important for WSe_2, especially for the lower polariton.

This thesis is organized in the following way. First, we introduce the theoretical framework in Chapter 2, in particular, we study the polariton dispersion and group velocity, which will be necessary for the following chapters. Then, we discuss the polariton-phonon scattering rates in Chapter 3. In Chapter 4, we investigate the polariton diffusion coefficient (Paper I). Next, in Chapter 5 we study the polariton absorption coefficient (Paper II). Finally, we end with a conclusion and future work prospects in Chapter 6.

CHAPTER 2

Theoretical Framework

In this chapter, we introduce the theoretical framework that constitutes the basis of this thesis. We start with the excitonic basis, the Wannier equation and present the excitonic Hamiltonian. From this, we can perform the Hopfield transformation and obtain the exciton-polariton Hamiltonian, with the new eigenmodes and eigenfunctions. Finally, we introduce the polariton equation of motion.

2.1 Excitons and the Wannier Equation

Semiconductor materials can be described as a many-particle system of interacting electrons, photons, and phonons. Hence, the Hamiltonian of said system in the second quantization includes: quasi-free electrons in a crystal lattice, photons, phonons, and electron-light, electron-phonon and photon-cavity interactions.

Due to the strong Coulomb interaction in TMDs, electrons and holes can form deeply bound pairs called excitons [3, 73, 74]. This can happen when the material absorbs a photon with energy higher than the bandgap, hence the electron is excited from the valence band to the conduction band leaving a hole in the latter. Excitons govern the optoelectronic properties of TMDs, even at room temperature [3, 75–78], due to this strong Coulomb interaction and exhibit a rich exciton landscape, including bright and dark exciton states [3, 39]. In particular the optical, as well as transport response, are often dominated by 1s excitons. Therefore, it is convenient to change from the electron-hole picture to an excitonic picture and restrict to 1s states, resulting in a drastic reduction of the number of states. From this, we can also decouple the relative and center of mass motion of the excitons and arrive at the Wannier equation.

Excitonic Basis

Let us consider the microscopic polarization $p^{v\uparrow c\uparrow}_{\mathbf{k}_1\mathbf{k}_2} = \langle \hat{a}^{\uparrow}_{v,\mathbf{k}_1} \hat{a}^{\uparrow}_{v,\mathbf{k}_2} \rangle$ and perform a change of variable: $p^{v\uparrow c\uparrow}_{\mathbf{k}_1\mathbf{k}_2} \rightarrow p^{vc}_{\mathbf{q}\mathbf{Q}}$ with $\mathbf{Q}$ center of mass and $\mathbf{q}$ relative momentum. This quantities are defined as: $\mathbf{Q} = \mathbf{k}_1 - \mathbf{k}_2$ and $\mathbf{q} = \alpha_\nu \mathbf{k}_1 + \beta_\nu \mathbf{k}_2$, with masses $\alpha_\nu = m_h/(m_h + m_e)$, $\beta_\nu = m_e/(m_h + m_e)$, m_h the hole mass and m_e the electron mass. Next, we want to decouple the relative movement from the center of mass one,

$$p^{v\uparrow c\uparrow}_{\mathbf{k}_1\mathbf{k}_2} \rightarrow p^{v\uparrow c\uparrow}_{\mathbf{q}\mathbf{Q}} = \sum_{\nu} \varphi^{\nu}_{\mathbf{q}} p^{\nu}_{\mathbf{Q}}, \tag{2.1}$$

where ν is the excitonic state, like the KK bright exciton. For the relative motion, we can solve the Schrödinger equation for an electron and a hole in momentum space, also commonly referred to as the Wannier equation,

$$\frac{\hbar^2 q^2}{2m^{\nu}_r} \varphi^{\nu}_{\mathbf{q}} - \sum_{\mathbf{k}} V^{exc}(\mathbf{k}) \varphi^{\nu}_{\mathbf{q}-\mathbf{k}} = \varepsilon_\nu \varphi^{\nu}_{\mathbf{q}}. \tag{2.2}$$

The eigenstates of this equation form a new brand new basis, showing in particular discretization in the relative momentum (i.e. $1s$, $2s$, etc). Note that the label ν of the excitonic state contains information on this discretization, however, in this thesis we only consider $1s$ states. Solving the Wannier

equation gives us access to the exciton eigen-energies ε_ν and eigenfunctions $\varphi^\nu_{\mathbf{q}}$. Importantly, these energies are quantized, showing values of. With these energies, we write the exciton center of mass dispersion as

$$E^{\mathrm{X}}_{\nu\mathbf{Q}} = E^\nu_g + \varepsilon_\nu + \frac{\hbar^2 Q^2}{2M^\nu}, \tag{2.3}$$

where E^ν_g is the single particle bandgap corresponding to valley ν.

Exciton Hamiltonian

We have introduced the exciton basis and excitons states, occupied by electron-hole pairs. If we continue to work on the electron picture basis, the calculations of equations of motion become lengthy as instead of working with the electron and hole momentum, we can simply have only one center-of-mass momentum of 1s excitons. Therefore, an alternative is to write the excitonic Hamiltonian, using the excitonic expansion scheme [79, 80]. Our new operators are $\hat{X}^\dagger_{\nu\mathbf{Q}}(\hat{X}_{\nu\mathbf{Q}})$, which creates and annihilates an exciton at state ν with center-of-mass momentum $\mathbf{Q}$. We can treat excitons as pure bosons if we work on the low-density limit. The exciton Hamiltonian includes also the exciton-photon and exciton-phonon interactions. For a more detailed approach to obtain the exciton Hamiltonian see [79, 81].

Let us start from defining an electron-hole pair operator $\hat{A}$, which combines conduction ($\hat{a}_c$) and valence ($\hat{a}_v$) band electrons as

$$\hat{A}_{\mathbf{k}\mathbf{k}'} = \hat{a}^\dagger_{c,\mathbf{k}}\hat{a}_{v,\mathbf{k}'} \tag{2.4}$$

and as we consider the low-density regime

$$\left[\hat{A}_{\mathbf{k}_1\mathbf{k}_2}, \hat{A}^\dagger_{\mathbf{k}_3\mathbf{k}_4}\right] \approx \delta_{\mathbf{k}_1\mathbf{k}_3}\delta_{\mathbf{k}_2\mathbf{k}_4} \tag{2.5}$$

we can obtain the fully bosonic commutation of electron-hole excitations. Therefore, the transformations to the Hamiltonian are

$$\hat{a}^\dagger_{c,\mathbf{k}}\hat{a}_{c,\mathbf{k}'} = \sum_{\mathbf{l}} \hat{A}^\dagger_{\mathbf{k}\mathbf{l}}\hat{A}_{\mathbf{k}'\mathbf{l}}, \qquad \hat{a}_{v,\mathbf{k}}\hat{a}^\dagger_{v,\mathbf{k}'} = \sum_{\mathbf{l}} \hat{A}^\dagger_{\mathbf{l}\mathbf{k}}\hat{A}_{\mathbf{l}\mathbf{k}'}. \tag{2.6}$$

This means we can transform the free and Coloumb Hamiltonian as free excitonic Hamiltonian

$$\sum_{i,\mathbf{k}} \varepsilon_{\mathbf{k}} \hat{a}^\dagger_{i,\mathbf{k}} \hat{a}_{i,\mathbf{k}} + \frac{1}{2} \sum_{ij,\mathbf{k}\mathbf{k}'\mathbf{q}} V_{\mathbf{q}} \hat{a}^\dagger_{i,\mathbf{k}+\mathbf{q}} \hat{a}^\dagger_{j,\mathbf{k}'-\mathbf{q}} \hat{a}_{j,\mathbf{k}'} \hat{a}_{i,\mathbf{k}} \rightarrow H^0_X = \sum_{\nu\mathbf{Q}} E^{\mathrm{X}}_{\nu\mathbf{Q}} \hat{X}^\dagger_{\nu\mathbf{Q}} \hat{X}_{\nu\mathbf{Q}}, \tag{2.7}$$

with $i, j = c, v$ valence and conduction band electrons and using also the expansion into excitonic eigenmodes

$$\hat{A}^\dagger_{\mathbf{k}_1\mathbf{k}_2} = \sum_{\nu} \hat{X}^\dagger_{\nu,\mathbf{k}_1-\mathbf{k}_2} \varphi(\alpha_\nu \mathbf{k}_1 + \beta_\nu \mathbf{k}_2), \tag{2.8}$$

which resembles the transformation of the polarization in equation (2.1). We can apply the same procedure to the electron-photon and electron-phonon Hamiltonian and in the end, we have

$$\begin{aligned} H_{\mathrm{X}} = &\sum_{\nu\mathbf{Q}} E^{\mathrm{X}}_{\nu\mathbf{Q}} \hat{X}^\dagger_{\nu\mathbf{Q}} \hat{X}_{\nu\mathbf{Q}} + \sum_{\nu\mathbf{Q}} g_{\mathbf{Q}} \left(\hat{c}^\dagger_{\mathbf{Q}} \hat{X}_{\nu\mathbf{Q}} + \hat{c}_{\mathbf{Q}} \hat{X}^\dagger_{\nu\mathbf{Q}} \right) \\ &+ \sum_{\nu\nu'\mathbf{Q}\alpha\mathbf{q}} \mathcal{D}^{\nu\nu'}_{\alpha\mathbf{q}} \hat{X}^\dagger_{\nu\mathbf{Q}+\mathbf{q}} \hat{X}_{\nu'\mathbf{Q}} (\hat{b}^\dagger_{\alpha,-\mathbf{q}} + \hat{b}_{\alpha\mathbf{q}}). \end{aligned} \tag{2.9}$$

The first term in the Hamiltonian characterizes the exciton kinetic motion with energy given by the equation (2.3). The second term expresses the exciton-light interaction mediated by the exciton-photon coupling matrix element $g_{\mathbf{Q}}$ [69, 82], where photons need to have the same in-plane momentum $\mathbf{Q}$ as excitons to fulfil the momentum conservation (hence restricting the coupling only to the bright exciton states within the light cone, i.e. $Q \approx 0$). Lastly, we have the exciton-phonon term [69], where the exciton-phonon coupling element is

$$\mathcal{D}^{\nu\nu'}_{\alpha\mathbf{q}} = D^c_{\alpha\mathbf{q}} \sum_{\mathbf{k}} \psi^{*\nu}(\mathbf{k}) \psi^{\nu'}(\mathbf{k} + \beta_\nu \mathbf{q}) - D^v_{\alpha\mathbf{q}} \sum_{\mathbf{k}} \psi^{*\nu}(\mathbf{k}) \psi^{\nu'}(\mathbf{k} - \alpha_\nu \mathbf{q}). \tag{2.10}$$

It describes the transition of an exciton from the state $(\nu, \mathbf{Q}) \rightarrow (\nu', \mathbf{Q} + \mathbf{q})$ aided by a phonon of mode α with relative momentum $\mathbf{q}$. The exciton-phonon coupling element is composed of the electron-phonon coupling element weighted by excitonic form factors $\sum_{\mathbf{k}} \psi^{*\nu}(\mathbf{k}) \psi^{\nu'}(\mathbf{k}+\mathbf{q})$. Parameters for phonons are found in [83], while electronic masses and other bandstructure parameters are found in [70].

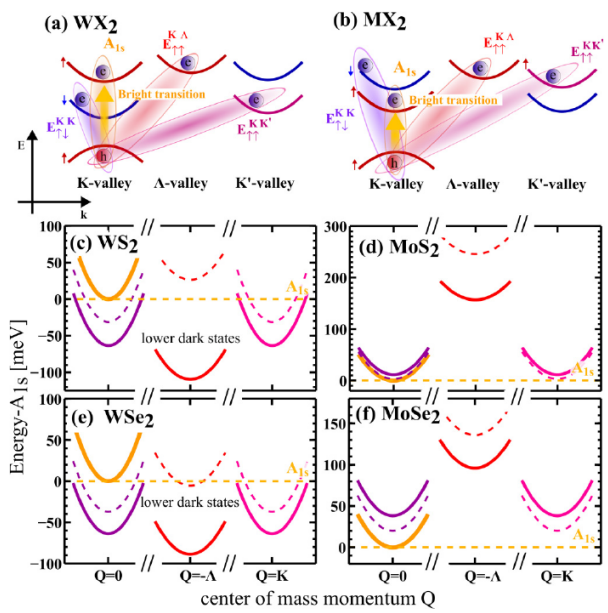

Figure 2.1: Excitonic Landscape for a hole in the K valley. Schematic representation of electronic dispersions around the K and valley for (a) tungsten-based TMDs (WS_2 and WSe_2) and (b) molybdenum-based TMDs (MoS_2 and $MoSe_2$). Exciton dispersion in (c) WS_2, (d) MoS_2, (e) WSe_2, and (f) $MoSe_2$ in SiO_2 substrate calculated by solving the Wannier equation. The figure is taken from [40].

Excitonic Landscape

As mentioned in the introduction, monolayers of transition metal dichalcogenides exhibit a considerable oscillator strength and exciton binding energies in the range of hundreds of meV, governing the optoelectronic properties of these materials [3, 75–78]. Hence, we briefly discuss the excitonic landscape, which includes bright, dark, and localized excitons. As we can see in Fig. 2.1, we have a variety of excitons. In this work, we focus on bright excitons and momentum-forbidden excitons. Bright excitons are states where the electron and hole have the same spin and momentum, i.e. they are both located around the K-point in the Brillouin zone, lying within the light cone and are referred to as KK excitons. These excitons are known as bright excitons as they can be accessed directly with light.

For dark excitons, the electron and hole have a different spin and/or momentum, ie., they are located in different valleys and/or can also have a different

spin, see Fig 2.1(a,b). We consider only momentum-forbidden dark excitons and with the hole always located in the K valley. Hence, the electron is located in a different valley, like in the high symmetry points Λ and K'. These excitons are called dark as they are inaccessible by light due to the required spin-flip and/or momentum transfer.

The energetic order of the different excitons is specific for each TMD, and even in the same material, the order can be changed e.g. by different substrates, which provide different binding energies for the different valleys. This means that if the dark excitons are not optically accessible, as they lie close to or even below the bright state, they can be possible scattering channels for the decay of excitons and influence the dynamics [65, 84]. For tungsten-based materials, the dark states are energetically below the bright state (see Fig. 2.1 (c) and (e)) and can influence the scattering channels and linewidth of the bright state [69, 85–87]. These dark states can also play an important role in the exciton-polariton scattering rates, optical spectra and dynamics.

2.2 Exciton-polaritons and Hopfield Transformation

This section discusses the central part of this thesis: the exciton-polariton. Here, we combine the density matrix formalism with the Hopfield approach [6]. In this thesis, the system in study is an hBN-encapsulated TMD monolayer integrated into an optical microcavity. Thus, we have photons inside, inner-cavity photons, and outside the cavity, outer-cavity photons. In Fig. 2.2 we have a schematic illustration of the system we study.

Let us first take the excitonic Hamiltonian from equation (2.9) and complete it with the necessary cavity terms. We quantize separately a single internal cavity mode of a Fabry-Perot resonator and the external radiation fields, which are split into two sets of continuum modes corresponding to the left

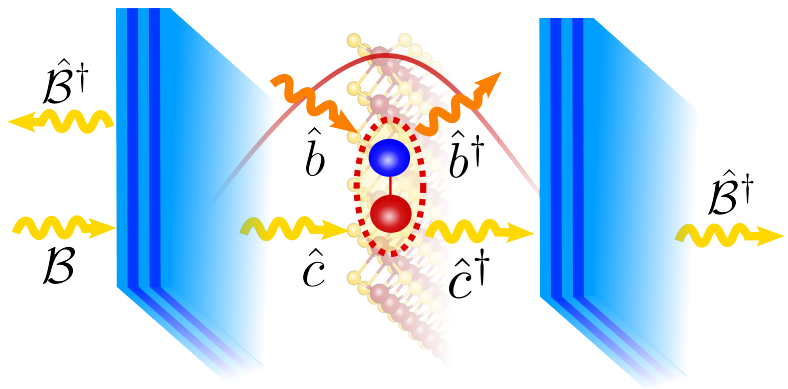

Figure 2.2: Schematic illustration of a TMD monolayer in a Fabry-Perot cavity with the fundamental cavity mode represented by the red curve. TMD excitons-polaritons interact with photons and phonons as indicated by the creation (annihilation) operators for photons ($\hat{c}^\dagger(\hat{c})$) and phonons ($\hat{b}^\dagger(\hat{b})$). The cavity system interacts with the outside world via the operators $\hat{\mathcal{B}}^\dagger(\hat{\mathcal{B}})$.

and the right of the cavity (Fig.2.2).

$$
\begin{aligned}
H_{\mathrm{X}} = &\sum_{\nu\mathbf{k}} E^{\mathrm{X}}_{\nu\mathbf{k}} \hat{X}^\dagger_{\nu\mathbf{k}} \hat{X}_{\nu\mathbf{k}} + \sum_{\mathbf{q}} E^{b}_{\alpha\mathbf{q}} \hat{b}^\dagger_{\alpha\mathbf{q}} b_{\alpha\mathbf{q}} + \sum_{\mathbf{k}} E^{\mathrm{c}}_{\mathbf{k}} \hat{c}^\dagger_{\mathbf{k}} \hat{c}_{\mathbf{k}} + \\
&+ \sum_{j=L,R} \sum_{\mathbf{k}} \int_0^\infty d\omega h\omega(\mathbf{k}) \hat{\mathcal{B}}^\dagger_{j\mathbf{k}\omega} \hat{\mathcal{B}}_{j\mathbf{k}\omega} \\
&+ \sum_{\nu\mathbf{k}} g_{\mathbf{k}} \left(\hat{c}^\dagger_{\mathbf{k}} \hat{X}_{\nu\mathbf{k}} + \hat{c}_{\mathbf{k}} \hat{X}^\dagger_{\nu\mathbf{k}} \right) + \sum_{\nu\nu'\mathbf{k}\alpha\mathbf{q}} \mathcal{D}^{\nu\nu'}_{\alpha\mathbf{q}} \hat{X}^\dagger_{\nu\mathbf{k}+\mathbf{q}} \hat{X}_{\nu'\mathbf{k}} (\hat{b}^\dagger_{\alpha,-\mathbf{q}} + \hat{b}_{\alpha\mathbf{q}}) + \\
&+ i\hbar \sum_{j=L,R} \sum_{\mathbf{k}} \int_0^\infty \frac{d\omega}{2\pi} a_{j,\mathbf{k}}(\omega) [\hat{\mathcal{B}}^\dagger_{j\omega\mathbf{k}} \hat{c}_{\mathbf{k}} - \hat{\mathcal{B}}_{j\omega\mathbf{k}} \hat{c}^\dagger_{\mathbf{k}}]. \qquad (2.11)
\end{aligned}
$$

The first four terms describe the free energy of excitons $E^{\mathrm{X}}_{\nu\mathbf{k}}$, phonons $E^{\mathrm{b}}_{\alpha\mathbf{q}}$ as well as the inner-cavity ($E^{\mathrm{c}}_{\mathbf{k}}$) and the outer-cavity ($\hbar\omega$) photons. Here, ν is the exciton index (we consider only 1s states), α the phonon mode, $\mathbf{k}$ and $\mathbf{q}$ are the in-plane momentum of excitons/photons (center-of-mass momentum for excitons) and phonons, respectively. Furthermore, we have $\hat{X}^\dagger_{\nu\mathbf{k}}(\hat{X}_{\nu\mathbf{k}})$, $\hat{b}^\dagger_{\alpha\mathbf{q}}(\hat{b}_{\alpha\mathbf{q}})$, $\hat{c}^\dagger_{\mathbf{k}}(\hat{c}_{\mathbf{k}})$, $\hat{\mathcal{B}}^\dagger_{j\mathbf{k}\omega}(\hat{\mathcal{B}}_{j\mathbf{k}\omega})$ as exciton, phonon, inner-cavity and outer-cavity photon creation (and annihilation) operators, respectively.

In the third line of equation (2.11), we have H_{x-c}, which describes the exciton-light interaction mediated by the exciton-photon coupling matrix

element $g_{\mathbf{k}}$ [69, 82]. In general, the out-of-plane component k_z influences the cavity energy and exciton-photon coupling. However, we assume the existence of one resonant photon mode (i.e., $E^{\mathrm{X}}_{KK,0} = E^{\mathrm{c}}_0$).

The next contribution in the Hamiltonian $\hat{H}_{X-b}$ describes the exciton-phonon interaction [69], where the coupling strength is determined by the exciton-phonon matrix element $\mathcal{D}^{\nu\nu'}_{\alpha\mathbf{q}}$. Finally, the last term provides the interaction between the inner- and outer-cavity photons [62, 72]. The free photons interact with the cavity with a coupling parameter, $a_{j,\mathbf{k}}(\omega)$. Assuming broadband end mirrors, taking the first Markov approximation and approximating this parameter as frequency independent [72] is appropriate. This contribution in the Hamiltonian leads to a consistent description of both the radiative decay rate within the cavity as well as the coupling of polaritons to input and output fields.

Now, we investigate the strong-coupling regime, where the exciton-photon coupling strength $g_{\mathbf{k}}$ has to be larger than the difference between the cavity and the non-radiative exciton decay rates [21]. This allows forming of polaritons as new eigenmodes of the system

$$\hat{Y}^n_{\mathbf{k}} = h^n_{\mathrm{X},\mathbf{k}}\hat{X}_{\mathbf{k}} + h^n_{\mathrm{c},\mathbf{k}}\hat{c}_{\mathbf{k}}, \tag{2.12}$$

where these polariton states consist of a coherent mixture of excitons and photons with the in-plane momentum $\mathbf{k}$, with the Hopfield coefficients $= h^n_{\mathrm{X},\mathbf{k}}/ = h^n_{\mathrm{c},\mathbf{k}}$ dictating this mixture. Applying this transformation, the Hopfield transformation, to the Hamilton operator yields [6, 21]

$$\begin{aligned}\hat{H} = &\sum_{\mathbf{k},n} E^n_{\mathbf{k}}\hat{Y}^{n\dagger}_{\mathbf{k}}\hat{Y}^n_{\mathbf{k}} + H^0_b + H^0_{\mathcal{B}} + \sum_{\mathbf{k}\alpha\mathbf{q}nn'} \tilde{\mathcal{D}}^{n'n}_{\mathbf{k}\alpha\mathbf{q}}\left(\hat{b}^\dagger_{\alpha,-\mathbf{q}} + \hat{b}_{\alpha\mathbf{q}}\right)\hat{Y}^{n'\dagger}_{\mathbf{k}+\mathbf{q}}\hat{Y}^n_{\mathbf{k}} + \\ &+ i\hbar\sum_{\mathbf{k},n,j}\int_0^\infty \frac{d\omega}{2\pi}a_{j\mathbf{k}}(\omega)\left(h^n_{C,\mathbf{k}}\hat{\mathcal{B}}^\dagger_{j\mathbf{k}\omega}\hat{Y}^n_{\mathbf{k}} - h^{n*}_{C,\mathbf{k}}\hat{\mathcal{B}}_{j\mathbf{k}\omega}\hat{Y}^{n\dagger}_{\mathbf{k}}\right).\end{aligned} \tag{2.13}$$

Here, the first term provides the free polaritonic Hamiltonian with $\hat{Y}^{n\dagger}_{\mathbf{k}}(\hat{Y}^n_{\mathbf{k}})$ denoting the polariton creation (annihilation) operator with polariton mode n and momentum $\mathbf{k}$. The energy of the corresponding polariton, $E^n_{\mathbf{k}}$, includes in particular lower and upper polariton branches (LP, UP) that are separated in $k = 0$ by the Rabi splitting $\hbar\Omega_R = E^{UP}_0 - E^{LP}_0$. Throughout this work, we focus on the resonant case, i.e. $E^{\mathrm{X}}_0 = E^{\mathrm{c}}_0$. In the strong coupling regime

with a large $g_{\mathbf{k}}$, an avoided crossing occurs and two polariton branches are formed. Their separation corresponds to the Rabi splitting $\hbar\Omega_{\mathrm{R}} = 2g_0$. The two polariton branches can be visualized in optical spectra for large-enough coupling g [88–90]. This is a consequence of mixing excitons and photons (with the same center-of-mass and total momentum), as quantified by the Hopfield coefficients, $h^n_{\mathrm{X},\mathbf{k}}$ and $h^n_{\mathrm{c},\mathbf{k}}$ [21]. We also include, for notation convenience, polaritons steaming from momentum-dark excitons, although these show no exciton-photon mixing. Nevertheless, we will show later their crucial role in the polariton absorption via additional phonon-induced scattering channels to the optically active polaritons. The second and the third term in Eq. (2.13) are the free phonon and free outer-cavity photon contributions, respectively, which are not affected by the Hopfield transformation. The fourth term describes the interaction of polaritons with the outer-cavity photons, mediated by the photonic Hopfield coefficients as only the photonic part of polaritons couples to the external radiation field. Finally, the last term in Eq. (2.13) describes the polariton-phonon interaction. Here, the matrix element $\tilde{D}$ is related to the exciton-phonon coupling via $\tilde{\mathcal{D}}^{n'n}_{\mathbf{k}\alpha\mathbf{q}} = h^{n'*}_{\mathrm{X},\mathbf{k}+\mathbf{q}}\mathcal{D}^{n'n}_{\alpha\mathbf{q}}h^n_{\mathrm{X},\mathbf{k}}$ and depends on the excitonic Hopfield coefficients h_X [91], since phonons only couple to the excitonic part of polaritons.

Polariton Dispersion

Now, we investigate the change of the excitonic band structure in the presence of a strong coupling regime. Both polariton energies $E^n_{\mathbf{k}}$ (Figure 2.3(a)) and Hopfield coefficients $h^n_{\mathrm{X},\mathbf{k}}$ and $h^n_{\mathrm{c},\mathbf{k}}$ (Figure 2.3(b)) can be obtained analytically (with subscript X and c referring to exciton and intra-cavity photon component, respectively) [21].

$$E^{\mathrm{LP/UP}}_{\mathbf{k}} = \frac{1}{2}E^{\mathrm{X}}_{\mathbf{k}} + \frac{1}{2}E^{\mathrm{c}}_{\mathbf{k}} \mp \frac{1}{2}\sqrt{4g^2_{\mathbf{k}} + \Delta E^2_{\mathbf{k}}} \tag{2.14}$$

with $\Delta E_{\mathbf{k}} = E^{\mathrm{X}}_{\mathbf{k}} - E^{\mathrm{c}}_{\mathbf{k}}$ and the Hopfield coefficients $h^{\mathrm{LP}}_{\mathrm{X},\mathbf{k}} = h^{\mathrm{UP}}_{\mathrm{c},\mathbf{k}} = C_{+,\mathbf{k}}$ and $h^{LP}_{\mathrm{c},\mathbf{k}} = -h^{UP}_{\mathrm{X},\mathbf{k}} = C_{-,\mathbf{k}}$ [6, 21], where

$$|C_{\pm,\mathbf{k}}|^2 = \frac{1}{2}\left(1 \pm \Delta E_{\mathbf{k}}\left[\Delta E^2_{\mathbf{k}} + 4g^2_{\mathbf{k}}\right]^{-\frac{1}{2}}\right). \tag{2.15}$$

For a vanishing exciton-phonon coupling $g_{\mathbf{k}}$, the lower/upper polariton branch approaches the cavity and exciton energy (thin yellow and grey lines in Fig.

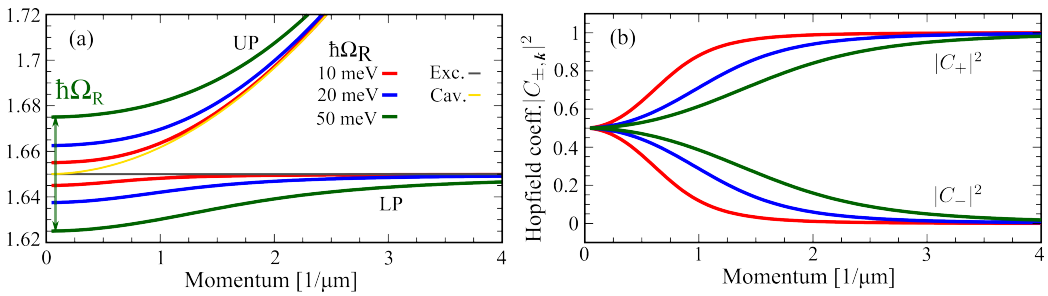

Figure 2.3: (a) Polariton dispersion and (b) Hopfield coefficients for three typical values of Rabi splitting. The bare exciton and photon energy are shown for comparison with thin grey and yellow lines, respectively.

2.3(a)), respectively.

Figure 2.3(a) illustrates the polariton dispersion for three values of the Rabi splitting representing different exciton-photon coupling strengths. The latter depends on the material's oscillator strength and the optical cavity's characteristics. We investigate the polariton dispersion for typical Rabi splitting values of $\hbar\Omega_{\mathrm{R}}$ =10, 25, 50 meV [29], which are larger than the non-radiative exciton linewidth (typically a few meV at low temperatures for hBN-encapsulation TMDs [69, 92, 93]) and the cavity linewidth (ranging from the meV [28] down to the μeV range [11, 94]), thus allowing for strong-coupling regime [21]. At larger momenta, the LP and UP branches merge with the exciton and photon dispersion, respectively. The larger $\hbar\Omega_{\mathrm{R}}$, the higher the momentum values at which this occurs, cf. Fig. 2.3(a). Polaritons are coherent superpositions of excitonic and photonic states with the Hopfield coefficients defining the weights of the single constituents, cf. Fig. 2.3(b). The coefficient $|C_{+,\mathbf{k}}|^2$ gives the exciton content of the lower polariton and the photon content of the upper polariton, i.e. for $|C_{+,\mathbf{k}}|^2$ =1 the LP state $|\mathrm{LP},\mathbf{k}\rangle = \hat{Y}_{\mathbf{k}}^{\mathrm{LP}\dagger}|0\rangle$ coincides with the exciton state $|\mathrm{X},\mathbf{k}\rangle$ and the UP state $|\mathrm{UP},\mathbf{k}\rangle$ corresponds to the photon state $|\mathrm{c},\mathbf{k}\rangle$.

Polariton Group Velocity and Occupation

From the polariton energies (2.14), we can calculate the polariton group velocity and the polariton band occupation. In Fig. 2.4, we consider the

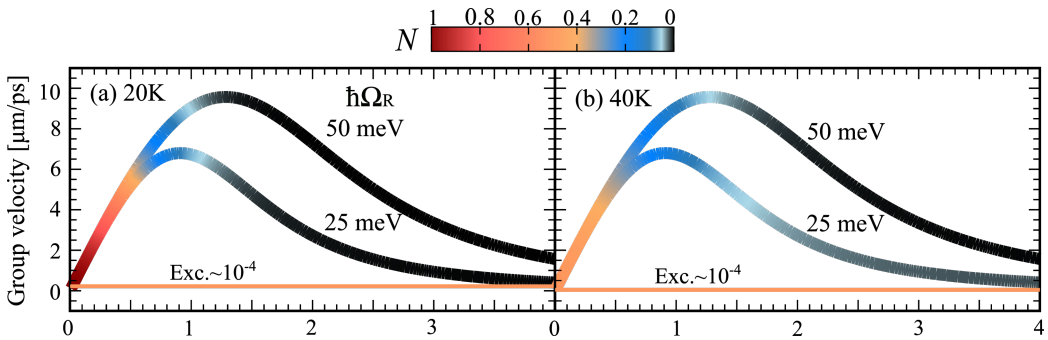

Figure 2.4: Lower polariton group velocity at (a) T=20 K and (b) T=40 K for two different Rabi splittings of $\hbar\Omega_R = 25$ and 50 meV. The corresponding band occupation is overlaid on the polariton dispersion, see the colour map. For comparison, the excitonic group velocity is shown by the thin orange line.

polariton group velocity given by

$$v_{\mathbf{k}}^n = \hbar^{-1}\frac{dE_{\mathbf{k}}^n}{d\mathbf{k}}, \tag{2.16}$$

in particular focusing on the lower polariton branch, since the upper one has a negligible occupation. We consider the two cases of Rabi splitting $\hbar\Omega_{\mathrm{R}}$=25, 50 meV for the polariton group velocity and compare it with the excitonic group velocity $v_k^X = \hbar k/M_X$, where M_X is the exciton mass. We find that the polariton group velocity is approximately 4 to 5 orders of magnitude larger than the excitonic one for small momenta within the light cone, cf. Fig. 2.4. Due to the rapidly changing polariton dispersion, we find group velocities in the range of 10 μm/ps, thus principally opening the possibility of ballistic polariton propagation for 10μ. This has recently indeed been observed in space- and angle-resolved photoluminescence experiments on a WS_2 monolayer in a distributed Bragg reflector cavity [13]. In addition to the remarkable magnitude difference, the group velocity for polaritons also has a qualitatively different momentum dependence. It shows a maximum in correspondence to the inflexion point in the lower polariton branch and decreases toward the excitonic velocity for momenta of several $\mu\mathrm{m}^{-1}$. In short, two subsets of states with considerably different group velocities coexist in a cavity: The fast ones located within the light cone and the slow ones outside of it coinciding with conventional excitons. Next, we overlay the occupation of the lower polariton state on the line displaying the group velocity (reddish colours denote large occupation), cf. Fig. 2.4, assuming a thermalized

Boltzmann distribution

$$f^n_{\mathbf{k}} \propto e^{-E^n_{\mathbf{k}}/k_B T}. \tag{2.17}$$

While the excitonic occupation is momentum-independent in the considered range of momenta (cf. the thin orange line in Fig. 2.4), strong variations are observed for polaritons. At 20 K, the occupation of the states at larger momenta is decreased by two orders of magnitude with respect to the exciton case for both considered Rabi splittings ($f^{\mathrm{LP}}/f^{\mathrm{X}} \approx 10^{-5}$ at $k \approx 4\mu\mathrm{m}^{-1}$), cf. orange vs black colour in Fig. 2.4. The curvature of the polariton branch induces a significant decrease in the occupation of the slow quasi-excitonic states at large momenta, as the energetically lower states at $k \approx 0$ are more efficiently populated. Increasing the temperature, the population of the former starts to increase, particularly for the smaller Rabi splitting of 25 meV, cf. Fig. 2.4(b). Regarding the behaviour at smaller momenta, we see that at 20 K, the occupation of states with the maximum group velocity is negligible for $\hbar\Omega_{\mathrm{R}}$=50 meV (black colour at approximately $k \approx 1.3\mu\mathrm{m}^{-1}$). However, when increasing the temperature to 40 K, we find a considerable occupation even at these states, indicating the possibility of a strongly accelerated polariton diffusion. We will discuss the diffusion coefficient in chapter 4.

Heisenberg Equations of Motion for Polaritons

Until now, we have worked in the Schrödinger picture, where the operators are constant in time. However, the Hamiltonian can give us access to the time dynamics of the system. To accomplish that, we change into the Heisenberg picture, and we find the time evolution of an observable (or, in our case, the expectation value) is determined by the equation of motion

$$i\hbar \frac{d\langle \mathcal{O} \rangle}{dt} = \langle [H, \mathcal{O}] \rangle \tag{2.18}$$

Now, we want to calculate the polariton dynamics. We start from the Heisenberg equations of motion for the coherent population of polariton, and external radiation field, taking their expectation values. For this, we make a correlation expansion including the dynamics of the phonon-assisted polarization. We consider a coherent calculation, i.e. the input laser is coherent and creates a coherent population of polaritons $\langle Y \rangle = Y \neq 0$, but not coher-

ent phonons, i.e. $\langle b\rangle = 0$. Hence, the equations of motion are

$$i\hbar\frac{d}{dt}\hat{Y}^n_{\mathbf{k}}(t) = E^n_{\mathbf{k}}\hat{Y}^n(t) - i\hbar\sum_{j=\mathrm{L,R}}\sum_{\mathbf{k}}\int_0^\infty\frac{d\omega}{2\pi}a_{j,\mathbf{k}}(\omega)h^n_{\mathrm{c},\mathbf{k}}\langle\mathcal{B}_{j\mathbf{k}}(t)\rangle+$$
$$+\hbar\sum_{\mathbf{q},n',n}\tilde{\mathcal{D}}^{n'n}_{\mathbf{k}\alpha\mathbf{q}}\langle\hat{Y}^{n'}_{\mathbf{k}-\mathbf{q}}(t)\left(\hat{b}^\dagger_{\alpha,-\mathbf{q}}(t)+\hat{b}_{\alpha\mathbf{q}}(t)\right)\rangle, \tag{2.19}$$

$$i\hbar\frac{d}{dt}\langle\hat{\mathcal{B}}_{j\mathbf{k}\omega}(t)\rangle = \langle[\hat{\mathcal{B}}_{j\mathbf{k}},\hat{H}]\rangle = \hbar\omega\hat{\mathcal{B}}^\dagger_{j\mathbf{k}\omega}(t) + i\hbar a_{j,\mathbf{k}}(\omega)\sum_n h^n_{\mathrm{c},\mathbf{k}}\hat{Y}^n_{\mathbf{k}}(t), \tag{2.20}$$

$$i\hbar\frac{d}{dt}\langle\hat{b}_{\alpha\mathbf{q}}(t)\rangle = \langle[\hat{b}_{\alpha\mathbf{q}},\hat{H}]\rangle = \hbar\sum_{n,n'\mathbf{k}}\tilde{D}^{n'n}_{\alpha,-\mathbf{q}}\langle\hat{Y}^{n,\dagger}_{\mathbf{k}-\mathbf{q}}(t)\hat{Y}^n_{\mathbf{k}}(t)\rangle = 0, \tag{2.21}$$

$$i\hbar\frac{d}{dt}S^{+,n}_{\mathbf{k}\alpha\mathbf{q}}(t) = \left(E^n_{\mathbf{k}-\mathbf{q}} - E^b_{\alpha\mathbf{q}}\right)S^{+,n}_{\mathbf{k}\alpha\mathbf{q}}(t) + \hbar\sum_{n'}\tilde{\mathcal{D}}^{n'n}_{\mathbf{k}\alpha,-\mathbf{q}}n^b_{\alpha\mathbf{q}}\hat{Y}^{n'}_{\mathbf{k}}(t), \tag{2.22}$$

$$i\hbar\frac{d}{dt}S^{-,n}_{\mathbf{k}\alpha\mathbf{q}}(t) = \left(E^n_{\mathbf{k}-\mathbf{q}} + E^b_{\alpha\mathbf{q}}\right)S^{-,n}_{\mathbf{k}\alpha\mathbf{q}}(t) + \hbar\sum_{n'}\tilde{\mathcal{D}}^{n'n}_{\mathbf{k}\alpha,-\mathbf{q}}n^b_{\alpha\mathbf{q}}\hat{Y}^{n'}_{\mathbf{k}}(t), \tag{2.23}$$

where n characterizes each polariton branch and $S^{+/-,n}_{\mathbf{k}}$ is the phonon-assisted polarizations . Next, we write a formal solution for the photon bath operator in terms of an arbitrary initial time solution t_0 with $t > t_0$. This operator depends on the state of the bath at a time t_0 and on the past history of the polaritons, i.e. they are leaking light into the photonic reservoir. We find

$$\hat{\mathcal{B}}_{j\mathbf{k}\omega}(t) = \hat{\mathcal{B}}_{j\mathbf{k}\omega}(t_0)e^{-i\omega(t-t_0)} + a_j(\omega)\sum_i h^n_{\mathrm{c},\mathbf{k}}\int_{t_0}^t dt'\hat{Y}^n_{\mathbf{k}}e^{-i\omega(t-t')}. \tag{2.24}$$

Inserting this solution into the second term of Eq. (2.19) and assuming that the coupling parameter $a_{j,\mathbf{k}}(\omega) = \sqrt{\kappa_{j,\mathbf{k}}/2}$ is not frequency dependent [72], we obtain

$$i\hbar h^n_{\mathrm{c},\mathbf{k}}\sum_{\mathbf{k},j=\mathrm{L,R}}\int_0^\infty\frac{d\omega}{2\pi}a_{j,\mathbf{k}}(\omega)\langle\mathcal{B}_{j\mathbf{k}\omega}(t)\rangle = -\left(\kappa_{\mathrm{L},\mathbf{k}}+\kappa_{\mathrm{R},\mathbf{k}}\right)\sum_{n'}h^{n,*}_{\mathrm{c},\mathbf{k}}h^{n'}_{\mathrm{c},\mathbf{k}}\hat{Y}^{n'}_{\mathbf{k}}(t)$$
$$+h^{n,*}_{\mathrm{c},\mathbf{k}}\sqrt{2\kappa_{\mathrm{L},\mathbf{k}}}b_{1,\mathbf{k}}(t) - h^{n,*}_{\mathrm{c},\mathbf{k}}\sqrt{2\kappa_{\mathrm{R},\mathbf{k}}}b_{2,\mathbf{k}}(t). \tag{2.25}$$

with the input fields

$$b_{1,\mathbf{k}}(t) = -\int_{-\infty}^\infty\frac{d\omega}{2\pi}\hat{\mathcal{B}}_{L\mathbf{k}\omega}(t_0)e^{-i\omega(t-t_0)}, \quad b_{2,\mathbf{k}}(t) = \int_{-\infty}^\infty\frac{d\omega}{2\pi}\hat{\mathcal{B}}_{R\mathbf{k}\omega}(t_0)e^{-i\omega(t-t_0)}. \tag{2.26}$$

To calculate the third term in Eq. (2.19), we need to determine the dynamics of the phonon-assisted polarizations $S^{+,n}_{\mathbf{k}\alpha\mathbf{q}}(t) = \langle \hat{Y}^n_{\mathbf{k}-\mathbf{q}} b^\dagger_{\alpha,-\mathbf{q}} \rangle$ and $S^{-,n}_{\mathbf{k}\alpha\mathbf{q}}(t) = \langle \hat{Y}^n_{\mathbf{k}-\mathbf{q}} b_{\alpha\mathbf{q}} \rangle$ appearing in Eqs. (2.22) and (2.23). These can be formally solved within the Markov approximation yielding [91]

$$S^{+,n}_{\mathbf{k}\alpha\mathbf{q}}(t) = -i\pi \sum_{n'} \tilde{\mathcal{D}}^{n'n}_{\mathbf{k}\alpha,-\mathbf{q}} n^b_{\alpha\mathbf{q}} \hat{Y}^{n'}_{\mathbf{k}}(t) \delta(\omega^{n'}_{\mathbf{k}} - \omega^n_{\mathbf{k}-\mathbf{q}} + \omega^b_{\alpha q}), \tag{2.27}$$

$$S^{-,n}_{\mathbf{k}\alpha\mathbf{q}}(t) = -i\pi \sum_{n'} \tilde{\mathcal{D}}^{n'n}_{\mathbf{k}\alpha,-\mathbf{q}} (1 + n^b_{\alpha\mathbf{q}}) \hat{Y}^{n'}_{\mathbf{k}}(t) \delta(\omega^{n'}_{\mathbf{k}} - \omega^n_{\mathbf{k}-\mathbf{q}} - \omega^b_{\alpha q}). \tag{2.28}$$

Furthermore, we determine the dynamics of the coherent polariton amplitude

$$i\hbar \frac{d}{dt} \hat{Y}^n_{\mathbf{k}}(t) = -\frac{i}{\hbar} E^n_{\mathbf{k}} \hat{Y}^n_{\mathbf{k}}(t) - \sum_{n'} [h^{n,*}_{\mathrm{c},\mathbf{k}} h^{n'}_{\mathrm{c},\mathbf{k}} (\kappa_{\mathrm{L},\mathbf{k}} + \kappa_{\mathrm{R},\mathbf{k}} + i\hbar \Gamma^{n',n}_{\mathbf{k}}] \hat{Y}^{n'}_{\mathbf{k}}(t) \tag{2.29}$$

and in the limit of a perfect cavity, $\kappa_L = \kappa_R = 0$, we find [91]

$$\frac{d}{dt} \hat{Y}^n_{\mathbf{k}}(t) = -\frac{i}{\hbar} E^n_{\mathbf{k}} \hat{Y}^n_{\mathbf{k}}(t) - \sum_{n'} \Gamma^{n',n}_{\mathbf{k}} \hat{Y}^{n'}_{\mathbf{k}}(t), \tag{2.30}$$

where $\Gamma^{n',n}_{\mathbf{k}}$ is the polariton-phonon scattering rate. Assuming that phonons do not induce oscillations between different polaritons, we obtain

$$\begin{aligned} i\hbar \frac{d}{dt} \hat{Y}^n_{\mathbf{k}}(t) = {} & (E^i_{\mathbf{k}} - i\hbar \Gamma^n_{\mathbf{k}}) \hat{Y}^n_{\mathbf{k}}(t) - i\hbar \sum_{n'} [h^{n,*}_{\mathrm{c},\mathbf{k}} h^{n'}_{\mathrm{c},\mathbf{k}} (\kappa_{\mathrm{L},\mathbf{k}} + \kappa_{\mathrm{R},\mathbf{k}})] \hat{Y}^{n'}_{\mathbf{k}}(t) \\ & + i\hbar h^{n,*}_{\mathrm{c},\mathbf{k}} \sqrt{2\kappa_{\mathrm{L},\mathbf{k}}} b_{1,\mathbf{k}}(t) - i\hbar h^{n,*}_{\mathrm{c},\mathbf{k}} \sqrt{2\kappa_{\mathrm{R},\mathbf{k}}} b_{2,\mathbf{k}}(t) \end{aligned} \tag{2.31}$$

This equation is similar to the expression found in Ref. [62], except that we have an additional term describing distinct phonon-induced damping for each polariton. Neglecting the excitation from the right-hand side of the cavity and performing the Fourier transform yields

$$\hat{Y}^n_{\mathbf{k}}(\hbar\omega) = \frac{-\hbar \sum_{n'} [h^{n,*}_{\mathrm{c},\mathbf{k}} h^{n'}_{\mathrm{c},\mathbf{k}} (\kappa_{\mathrm{L},\mathbf{k}} + \kappa_{\mathrm{R},\mathbf{k}})] \hat{Y}^{n'}_{\mathbf{k}}(\omega) + \hbar h^{n,*}_{\mathrm{c},\mathbf{k}} \sqrt{2\kappa_{\mathrm{L},\mathbf{k}}} b_{1,\mathbf{k}}(t)}{i(E^n_{\mathbf{k}} - \hbar\omega) + \hbar \Gamma^n_{\mathbf{k}}} \tag{2.32}$$

with the polariton scattering rates

$$\Gamma^n_{\mathbf{k}} = 2\pi \sum_{n'\alpha\mathbf{k}'} |\tilde{\mathcal{D}}^{n',n}_{\alpha,\mathbf{k}-\mathbf{k}'}|^2 \left(\frac{1}{2} \pm \frac{1}{2} + n^b_{\alpha,\mathbf{k}-\mathbf{k}'} \right) L_{\tilde{\gamma}_0} \left(E^{n'}_{\mathbf{k}'} - E^k_{\mathbf{k}} \pm \hbar\omega^b_{\alpha,\mathbf{k}-\mathbf{k}'} \right), \tag{2.33}$$

with $\tilde{\mathcal{D}}^{n',n}_{\alpha,\mathbf{k}-\mathbf{k}'}$ the polariton-phonon matrix element, $n^b_{\alpha,\mathbf{k}-\mathbf{k}'}$ the Bose-Einstein distribution, $\hbar\omega^b_{\alpha,\mathbf{k}-\mathbf{k}'}$ the phonon energy of the mode α with momentum $\mathbf{q} = \mathbf{k}' - \mathbf{k}$, and $L_{\tilde{\gamma}_0}(\hbar\omega)$ the Lorentzian function with a broadening $\tilde{\gamma}_0$,

$$L_{\tilde{\gamma}_0}(\hbar\omega) = \frac{1}{\pi}\frac{\tilde{\gamma}_0}{\tilde{\gamma}_0^2 + \hbar\omega^2}. \tag{2.34}$$

This result is similar to the exciton scattering rates [82, 95], where one can replace the exciton energies with the polaritons ones and the exciton-phonon matrix element with the renormalized polariton-phonon matrix element. This is due to only the excitonic part of the polariton coupling to the phonons.

CHAPTER 3

Phonon-induced Scattering Rates

In this chapter, we turn our focus on the phonon-induced polariton scattering rates. These serve as a basis for the discussion in the next chapters, as they are one of the key pieces for the diffusion coefficient and the polariton optical absorption.

Let us start by retrieving the polariton-phonon scattering rate, calculated in chapter 2,

$$\Gamma^n_{\mathbf{k}} = 2\pi \sum_{n'\alpha\mathbf{k}'} |\tilde{\mathcal{D}}^{n',n}_{\alpha,\mathbf{k}-\mathbf{k}'}|^2 \left(\frac{1}{2} \pm \frac{1}{2} + n^b_{\alpha,\mathbf{k}-\mathbf{k}'}\right) L_{\tilde{\gamma}_0}\left(E^{n'}_{\mathbf{k}'} - E^n_{\mathbf{k}} \pm \hbar\omega^b_{\alpha,\mathbf{k}-\mathbf{k}'}\right) \tag{3.1}$$

where $\tilde{\mathcal{D}}^{n',n}_{\alpha,\mathbf{k}-\mathbf{k}'}$ is the polariton-phonon matrix element, $n^b_{\alpha,\mathbf{k}-\mathbf{k}'}$ the Bose-Einstein distribution, $\hbar\omega^b_{\alpha,\mathbf{k}-\mathbf{k}'}$ the phonon energy of the mode α with momentum $\mathbf{q} = \mathbf{k}' - \mathbf{k}$, and $L_{\tilde{\gamma}_0}(\hbar\omega)$ the Lorentzian function with a broadening $\tilde{\gamma}_0$. In our work, we partially include some effects beyond the so-called

completed-collision limit [96] introducing a Lorentzian function instead of a Delta function. This is similar to the damping introduced in the second-order Born approximation, including higher-order effects leading e.g. to a collisional broadening [97, 98]. We use the value of 0.1 meV, which provides a low estimation of the scattering rates.

Considering the diverse excitonic landscape, we divide the chapter into two sections. First, we discuss the intra-valley scattering in the KK valley and then move to the inter-valley scattering by adding the Λ and K' valleys. We neglect the scattering with defects/disorder [13].

3.1 Intra-valley Scattering

First, we start with the intra-valley polariton-phonon scattering rates, which we plot in Fig. 3.1 for a temperature of 40K. We choose this temperature as we see interesting physics around this temperature point, which will be discussed in detail in chapter 4. Note that only the scattering into LP states out of the light cone is efficient due to the limited number of receiving partner states available that exist within the light cone as well as due to the negligibly small Hopfield coefficient $h_{\mathrm{X}}^{\mathrm{UP}}$ for large-momenta UP states. This implies that the receiving LP state is quasi-excitonic, cf. Fig. 2.3, i.e. the associated coefficient $h_{\mathrm{X}}^{\mathrm{LP}} \approx 1$, as the scattering with phonons is driven by the excitonic component of the emitting polariton. With this in mind, one would expect larger scattering rates for LP states, as the excitonic constituent is dominant in the polariton. Surprisingly, our microscopic calculations of scattering rates show a much more efficient scattering for the UP branch, cf. Fig. 3.1(b), which we will explain below.

Let us first discuss the LP scattering rates for $MoSe_2$ shown in Fig. 3.1(a). For states around k=0, we find two orders of magnitude smaller polariton-phonon scattering compared to the exciton case (thin black line), while the Hopfield coefficient $|C_+|^2 = 0.5$ would only imply a decrease by a factor of two. The reason for the dramatic decrease is related to the change in the dispersion relation in the strong coupling regime. The energy of acoustic phonons, $\hbar v_s k$, is smaller than the polariton on and appears to be almost flat due to the smaller velocity compared to the polariton group velocity (cf.

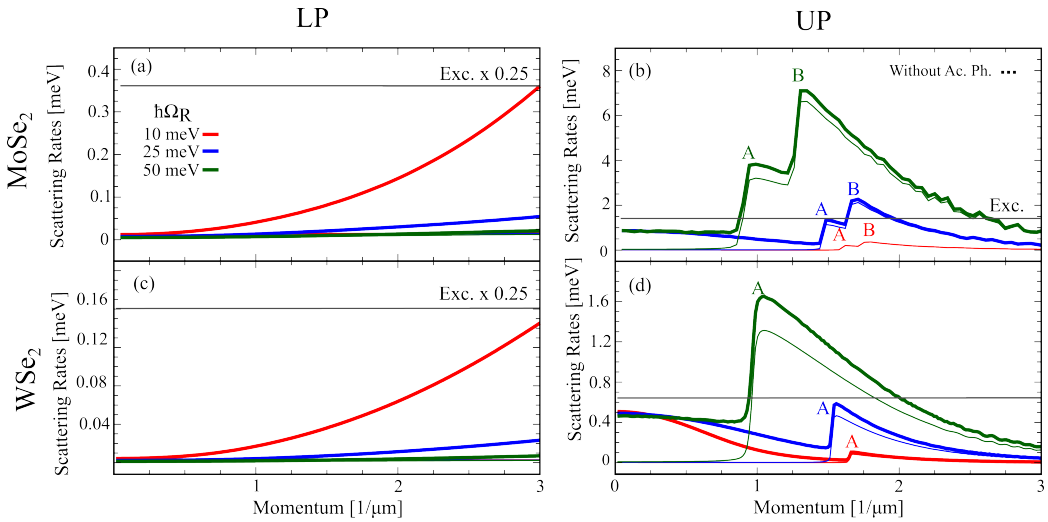

Figure 3.1: Polariton-phonon scattering rates at $T = 40$ K for (a) and (c) the lower polariton branch for $MoSe_2$ and WSe_2, respectively. (b) and (d) the upper polariton branch for $MoSe_2$ and WSe_2, respectively. Dashed lines show the case without the contribution of acoustic phonons. Note that in (a) and (c), all three dashed lines lie close to each other and are nearly momentum-independent, illustrating the crucial role of acoustic phonons for the increased scattering at large momenta.

orange and red line in Fig. 3.2(a), respectively). Consequently, when low-momentum polaritons absorb acoustic phonons, they are not able to find a resonant scattering partner. This is only possible if they are very close to the exciton energy E_0^X. The increase of the scattering rate at larger momenta can be traced back to non-resonant scattering with acoustic phonons (cf. the dashed line in Fig. 3.1(a) excluding acoustic phonons). This is due to the width of the Lorentzian in Eq. 3.1, whose origin can be related to higher-order scattering contributions inducing a softening of the energy selection rules. Note that the scattering rates show a quantitative dependence on this phenomenologically introduced width parameter. However, the qualitative behaviour remains unaffected. Looking at figure 3.1(c), which is for WSe_2, we can see that the tungsten material exhibits the same behaviour as $MoSe_2$ in Fig. 3.1(a). The difference is that in WSe2 the scattering rates are smaller than for $MoSe_2$ because the intravalley scattering in $MoSe_2$ is stronger than for WSe_2 as also seen for excitons.

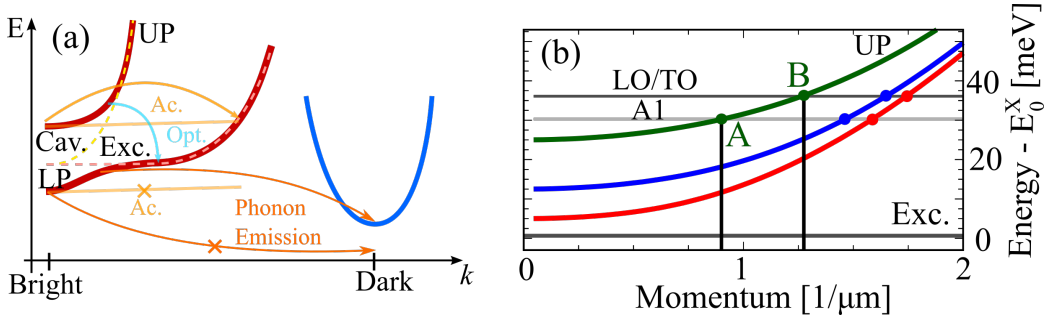

Figure 3.2: (a) Schematic representation of possible scattering channels induced by emission and absorption of acoustic and optical phonons. (b) Crossing points of optical phonon dispersion with the upper polariton branch for different $\hbar\Omega_R$ explaining the resonances appearing in Fig. 3.1(b).

Next, we discuss the UP scattering rates for $MoSe_2$, as we did for LP, illustrated in Fig. 3.1(b). At very small momenta, the scattering with acoustic modes is more efficient and reaches a value that is approximately only two times smaller than for excitons, as expected by the Hopfield coefficient (Fig. 2.3(b)). Since the UP branch is higher in energy compared to excitons, it is possible to find resonant scattering partners, cf. the crossing between the phonon dispersion (top orange line) and LP energy in Fig. 3.2 (a)). As a result, scattering via acoustic phonons is possible. At larger momenta, we observe the appearance of pronounced A and B resonances reflecting the emission of optical phonons. To better understand their origin, in Fig. 3.2(b) we plot the UP dispersion and the optical phonon energies (with respect to the exciton energy E_0^X) and find crossing points precisely at the position of the A and B peaks in the scattering rate. Note that the different weight of these peaks for different Rabi splitting is due to the Hopfield coefficients. For $\hbar\Omega$R=50 meV, the A peak appears at $k \approx 1\mu\text{m}^{-1}$, where $|C_+|^2 \approx 0.4$, while at 10 meV it appears at $k \approx 1.5\mu\text{m}^{-1}$ with $|C_+|^2 \approx 0.04$ resulting in a much smaller scattering efficiency. The UP scattering rates are dominated by resonant scattering. Hence the width of the Lorentzian plays a minor role. As in the case of $MoSe_2$, the scattering rates close to $k \approx 0$ for WSe_2 are dominated by acoustic modes and, in general, the behaviour of the curves is explained by the same arguments. We only see the appearance of one peak as the three optical modes are very close in energy ($\hbar\omega_{TO} = 30.5$ meV, $\hbar\omega_{LO,A1} = 30.8$ meV) However, in this material the optical emission is not as efficient as in the molybdenum case. Before, we had an increase of almost an order for the

$\hbar\Omega_R = 50$ meV case, while in Fig. 3.1(d) it only increases around 2 times. We can also see that the dashed lines in WSe_2 are more apart than for $MoSe_2$. The difference in magnitude is also reflected in the value of the bare exciton case as they differ by one order of magnitude. This difference between the two materials is due to the higher value of deformation potential for $MoSe_2$ [83].

In a nutshell, the polariton-phonon intra-valley scattering is strongly affected by the polariton dispersion resulting in suppressed scattering with acoustic phonons for LP and an enhanced emission of optical phonons for UP states.

3.2 Inter-valley Scattering

Now, we allow polaritons to scatter into the dark valleys. We explicitly consider it by including K' and Q' phonons, which allow scattering into polaritons coinciding with KK' and $K\Lambda$ excitons, respectively. Following the scheme in the previous section, in Figure 3.3 (a) and (c) we plot the lower polariton branch for $MoSe_2$ and WSe_2, while in (b) and (d) we plot the upper polariton. We again consider three values of Rabi splitting $\hbar\Omega_R = 10$, 25 and 50 meV, but this time for a temperature of 77 K. This time we choose the liquid point of nitrogen as we aim to approach our results to possible experimental setups. Let us start with $MoSe_2$. As discussed in chapter 2, this material is a direct band gap semiconductor hence, we expect a small contribution from the dark channels to the scattering rates, since the dark states are energetically above the bright state. Observing Fig. 3.3(a) and (b), we see that the thin lines (corresponding to the intravalley scattering) are very close to the thick lines (full scattering rates). In both branches for $\hbar\Omega_R = 10$ meV, we do not see a qualitative change in the behaviour of the curve, as dark excitons only slightly increase the magnitude of the scattering rates. As we increase the value of Rabi splitting, we can see the opening of emission channels into the dark valley with acoustic modes, as can be seen in Fig. 3.4. However, these contributions are small (especially when compared later with WSe_2, see discussion below).

Opposed to the intravalley case, we can find resonant scattering partners for the lower polariton with acoustic phonons in the dark valleys as these

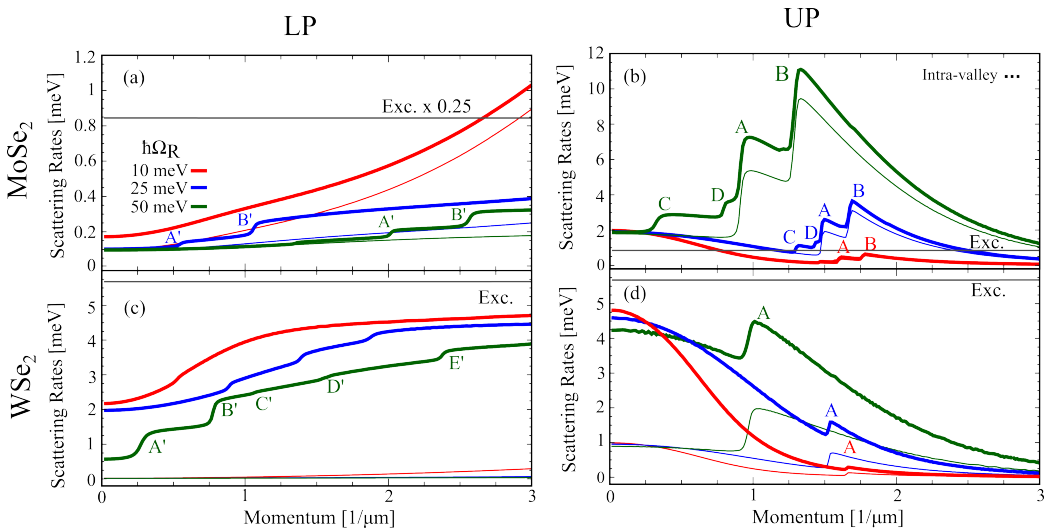

Figure 3.3: Polariton-phonon full scattering rates at $T = 77$ K for (a) and (c) the lower polariton branch for $MoSe_2$ and WSe_2, respectively. (b) and (d) the upper polariton branch for $MoSe_2$ and WSe_2, respectively. The thin lines show the case without the contribution of dark excitons. Note that in (a) and (b), all these thin lines lie close to the full contribution (thick lines).

phonons have a flat dispersion and are treated the same way as optical phonons. We see the two steps corresponding to the LA and TA acoustic phonons with energies $\hbar\omega_{LA} = 16.6$ meV and $\hbar\omega_{TA} = 19.9$ meV. In figure 3.4, we show the crossing of the phonon dispersion with the respective polariton, and it corresponds to the position of the marked steps in Fig. 3.3(a) and (b) (A′ and B′ for LP, and C and D for UP). In the upper polariton branch, we can also see crossing for the curves with $\hbar\Omega_R$=10, 25 meV, however, the corresponding peaks in Fig. 3.3(b) are quite weak, due to the Hopfield coefficients, as explained for the intravalley case.

Now, moving to WSe_2. In the upper polariton case, all the scattering channels into the dark valleys are open even from $k = 0$. Hence, the presence of dark excitons only increases the magnitude of the scattering, where the only peak A is due to the intravalley optical emission, as discussed in the previous section. For the lower polariton, we can see several step-like behaviours in the curves, as in the case of $MoSe_2$, and the scattering rates are hugely increased in magnitude. This means that the scattering from the lower polariton is

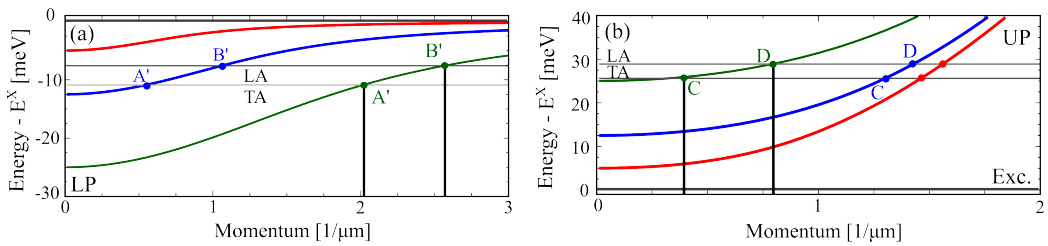

Figure 3.4: Crossing points of acoustic phonon dispersion for $MoSe_2$ with the lower (a) and upper polariton branch (b) for different $\hbar\Omega_R$ explaining the resonances appearing in Fig. 3.3(a) and (b), respectively.

no longer weak when we include the intervalley scattering. At momentum $k = 0$, the energy E_0^{LP} for $\hbar\Omega_R = 50$ meV of the lower polariton is too low to allow scattering into the KΛ exciton via emission of phonons (Fig. 3.2(a))) as $E_0^{LP} - E_{\Lambda,0}^X \approx 11.2$ meV, which is just smaller than the energy of 11.4 meV of intervalley TA phonons [83]. When k reaches the threshold value of $k \approx 0.3$ μm^{-1}, the scattering channel into $K\Lambda$ states opens, resulting in the abrupt increase of $\Gamma_{\mathbf{k}}^n$, cf. also the schematic in Fig. 3.2(a). The second step at k=0.8 also corresponds to the acoustic emission with a phonon energy of 14.3 meV. Acoustic emission into $K\Lambda$ dominates the $\hbar\Omega_R = 50$ meV curve, however, there are other step-like increases (although weaker). They correspond to optical emission into $K\Lambda$ valley (step E$'$ at k=2.4 μm^{-1}) and to KK' (steps C$'$ and D$'$). For $\hbar\Omega_R = 10$ (1 step) and 25 meV (3 steps) curves, the steps correspond to the opening of optical emission of phonons to the $K\Lambda$ valley with energies $\hbar\omega_{TO} = 27.3$ meV, $\hbar\Omega_{TO} = 32.5$ meV and, $\hbar\omega_{A1} = 30.4$ meV.

Next, we study the linewidth of the lower and upper polariton as a function of temperature for WSe_2 to see the impact of the dark excitons. In Figs. 3.5(a) and (b) we show the temperature-dependent for WSe_2 polariton-phonon scattering rates at $\mathbf{k} = 0$ for the UP and LP branches, respectively. We add up different scattering channels including intravalley scattering within the K valley (KK) and intervalley scattering into momentum-dark exciton states (KK' and $K\Lambda$). For both polariton branches, the most significant contribution to the linewidth comes from the intervalley scattering into dark $K\Lambda$ excitons reflecting the efficient scattering plus the three-fold degeneracy of the Λ valley, similar to the excitonic case [99]. Furthermore, intervalley scattering within the K valley is also essential at room temperature. At 20K, the LP linewidth is determined to a large extent by scattering into the dark

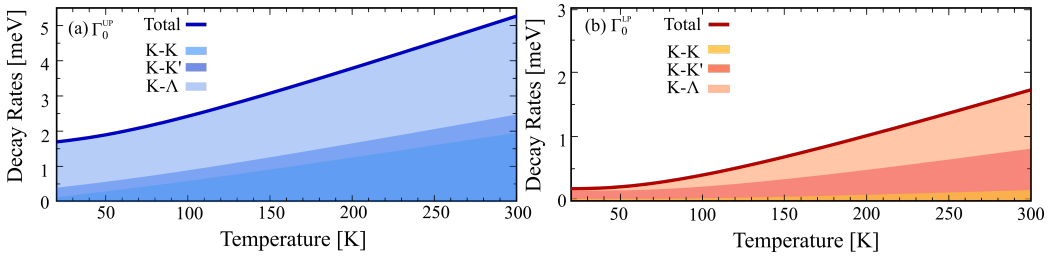

Figure 3.5: Temperature study for WSe_2. Polariton-phonon scattering rate $\Gamma^n_{\mathbf{k}}$ for the (a) upper (UP) and (b) lower polariton branch (LP) at $k = 0$ as a function of temperature (for $Q_f \approx$160). We identify the contributions of the intravalley (KK) as well as intervalley (KK', KΛ) scattering channels (shaded areas).

KK' excitons. We stress that here we focus on the scattering from the $k = 0$ polariton state. There are further possible scattering channels at larger momenta, as shown in Fig.3.4(c). Increasing the temperature to 300K increases the LP linewidth by around one order of magnitude as the absorption of intervalley phonons becomes possible. At 77 K the intravalley contribution to the phonon-scattering rates is very small, in accordance with Fig.3.3(c). The linewidth of the upper polariton is at 20K, much larger compared to the LP branch since emission into dark excitons is possible even at $k = 0$ thanks to the much higher polariton energy. Hence, the increase in UP from 20K to 300K is not as substantial as in the LP case. Overall, Figs. 3.5(a,b) illustrate the considerable impact of dark exciton states on the polariton-phonon scattering rates.

The study of the phonon-induced polariton scattering rates opens the door to the study of different polariton properties, like diffusion coefficient (see 4), which has been observed in other materials [63, 64]. In terms of optics, we can use this quantity to determine the absorption coefficient and study how dark exciton influence the polariton optical spectrum, as we will discuss in chapter 5.

CHAPTER 4

Diffusion

The transport of exciton-polaritons is strongly influenced by their excitonic nature. In this chapter, we introduce Paper I, where we focus the study on the polariton diffusion coefficient.

4.1 Theoretical Background

Polaritons, in general, show peculiar transient spatio-temporal dynamics resulting in a long ballistic propagation even at room temperature [13], as well as a non-linear transport behaviour [33, 34]. While full spatio-temporal polariton dynamics is beyond the scope of this thesis, we focus the investigation on polariton diffusion coefficients in the steady-state limit. In TMD monolayers, excitons show - after an initial unconventional diffusion [43, 45] - a regular steady-state diffusion behaviour, i.e. exhibiting a linear increase of the square width of the spatial distribution as a function of time [46, 100–

103]. The rate of this increase is given by the diffusion coefficient D [45, 104]. Such a regime appears when a local thermalized distribution is reached and when the scattering processes are fast enough, leading to a quick thermalization compared to the transport timescale [104].
The starting point to calculate the diffusion coefficient for polaritons is the same as for excitons, and it is defining the local distribution

$$f(\mathbf{k},\mathbf{r},t) = f_0(\mathbf{k},\mathbf{r},t) + \delta f(\mathbf{k},\mathbf{r},t) \tag{4.1}$$

where f_0 is in local quasi-equilibrium. From this, one defines the spatially-dependent current

$$\mathbf{J}(\mathbf{r},t) = \frac{1}{V}\sum_{n\mathbf{k}} \mathbf{v}^n_{\mathbf{k}} f(\mathbf{k},\mathbf{r},t) = \frac{1}{V}\sum_{n\mathbf{k}} \mathbf{v}^n_{\mathbf{k}} \delta f(\mathbf{k},\mathbf{r},t) \tag{4.2}$$

with $\mathbf{v}^n_{\mathbf{k}}$ the group velocity of the n polariton. Now, we define the Boltzmann equation, considering no losses

$$\partial_t f((\mathbf{k},\mathbf{r},t) = -v^n_{\mathbf{k}} \cdot \nabla_{\mathbf{r}} f(\mathbf{k},\mathbf{r},t) + d_t f(\mathbf{k},\mathbf{r},t)|_{scattering}, \tag{4.3}$$

where the first term on the right side of the equation gives the free evolution for isotropic parabolic dispersion and the last term provides the effect of scattering, which here we evaluate through the (spatially-local) Boltzmann collision term (for $f << 1$)

$$\begin{aligned} d_t f(\mathbf{k},\mathbf{r},t)|_{sca.} &= \left[\sum_{\mathbf{k}'} \left(\Gamma_{\mathbf{k}\mathbf{k}'} f(\mathbf{k}',\mathbf{r},t) - \Gamma_{\mathbf{k}'\mathbf{k}} f(\mathbf{k},\mathbf{r},t)\right)\right] = \\ &= \sum_{\mathbf{k}'} \left[\Gamma_{\mathbf{k}\mathbf{k}'} f_0(\mathbf{k}',\mathbf{r},t) - \Gamma_{\mathbf{k}'\mathbf{k}} f_0(\mathbf{k},\mathbf{r},t)\right] + \\ &+ \sum_{\mathbf{k}'} \Gamma_{\mathbf{k}\mathbf{k}'} \delta f(\mathbf{k}',\mathbf{r},t) - \left(\sum_{\mathbf{k}'} \Gamma_{\mathbf{k}'\mathbf{k}}\right) \delta f(\mathbf{k},\mathbf{r},t) \cong \qquad (4.4) \\ &\cong -\tau_{\mathbf{k}}^{-1} \delta f(\mathbf{k},\mathbf{r},t), \qquad (4.5) \end{aligned}$$

where the terms with $f_0(\mathbf{k},\mathbf{r},t)$ are zero by the definition of the quasi-equilibrium distribution, $\Gamma_{\mathbf{k}\mathbf{k}'}/\Gamma_{\mathbf{k}'\mathbf{k}}$ are the in/out-scattering rates, and since $\sum_{\mathbf{k}} \delta f(\mathbf{k},\mathbf{r},t) = 0$ the third term in equation (4.4) is much smaller than the last one. Inserting the result of Eq. (4.5) into equation (4.3) we have [104]

$$\delta f(\mathbf{k},\mathbf{r},t) = -\tau_{\mathbf{k}} \left[\partial_t f(\mathbf{k},\mathbf{r},t) + \mathbf{v}^n_{\mathbf{k}} \cdot \nabla_{\mathbf{r}} f(\mathbf{k},\mathbf{r},t)\right]. \tag{4.6}$$

In turn, inserting this equation into the current equation (4.2) with the approximation $f \approx f_0$

$$\mathbf{J}(\mathbf{r}) = \frac{1}{V}\sum_{n\mathbf{k}} \mathbf{v}^n_{\mathbf{k}}(-\tau_{\mathbf{k}})\partial_t f_0(\mathbf{k},\mathbf{r},t) - \frac{1}{V}\sum_{n\mathbf{k}} \tau_{\mathbf{k}}\mathbf{v}^n_{\mathbf{k}}\mathbf{v}^n_{\mathbf{k}} \cdot \nabla_{\mathbf{r}} f_0(\mathbf{k},\mathbf{r},t) = \tag{4.7}$$

$$= -\frac{1}{dV}\sum_{n\mathbf{k}} \tau_{\mathbf{k}}|v^n_{\mathbf{k}}|^2 \nabla_{\mathbf{r}} f_0(\mathbf{k},\mathbf{r},t), \tag{4.8}$$

where the first term in (4.7) is zero as the group velocity is an odd function while the other terms are even functions in momentum, hence when we sum over $\mathbf{k}$ this term is zero and d is the dimension of the system. Considering the completed collision limit, meaning $f << 1$,

$$f_0(\mathbf{k},\mathbf{r},t) \cong e^{-E^n_{\mathbf{k}}/k_BT} e^{\mu(\mathbf{r})/k_BT} \tag{4.9}$$

where $E^n_{\mathbf{k}}$ is the polariton energy, T the temperature, k_B the Boltzmann constant and from which it follows

$$\nabla_{\mathbf{r}} f_0(\mathbf{k},\mathbf{r},t) = \frac{1}{k_BT} e^{-E^n_{\mathbf{k}}/k_BT} e^{\mu(\mathbf{r})/k_BT} \nabla_{\mathbf{r}}\mu(\mathbf{r}) = \frac{f_0(\mathbf{k},\mathbf{r},t)}{k_BT}\nabla_{\mathbf{r}}\mu(\mathbf{r}) =$$

$$= -\frac{\partial f_0(\mathbf{k},\mathbf{r},t)}{\partial E^n_{\mathbf{k}}} \frac{\partial \mu(\mathbf{r})}{\partial N(\mathbf{r})} \nabla_{\mathbf{r}} N(\mathbf{r}) \tag{4.10}$$

and the current becomes simply

$$\mathbf{J} = -D\nabla_{\mathbf{r}} N(\mathbf{r}) \tag{4.11}$$

with

$$D = -\frac{1}{dV}\sum_{n\mathbf{k}} |v^n_{\mathbf{k}}|^2 \tau_{\mathbf{k}} \frac{\partial f_0(\mathbf{k},\mathbf{r},t)}{\partial E^n_{\mathbf{k}}} \frac{\partial \mu(\mathbf{r})}{\partial N(\mathbf{r})} \tag{4.12}$$

which coincides with the result in [104], considering an exciton dispersion $E^{\mathrm{X}}_k = \hbar^2 k^2/2m$ and a group velocity $v_{\mathbf{k}} = \hbar k/m$. Now, let us take the term

$$\frac{1}{V}\sum_{\mathbf{k}} f_0(\mathbf{k},\mathbf{r},t) = N(\mathbf{r}) = \frac{1}{V} e^{\mu(\mathbf{r})/k_BT} \sum_{\mathbf{k}} e^{-E^n_{\mathbf{k}}/k_BT} \tag{4.13}$$

hence

$$\frac{\partial f_0(\mathbf{k},\mathbf{r},t)}{\partial E^n_{\mathbf{k}}} = -\frac{1}{k_BT} f_0(\mathbf{k},\mathbf{r},t) = -\frac{1}{k_BT}\frac{N(\mathbf{r})e^{-E^n_{\mathbf{k}}/k_BT}}{V^{-1}\sum_{\mathbf{k}} e^{-E^n_{\mathbf{k}}/k_BT}} \tag{4.14}$$

$$\frac{\partial \mu(\mathbf{r})}{\partial N(\mathbf{r})} = \frac{k_BT}{N(\mathbf{r})} \tag{4.15}$$

and, finally, [104]

$$D = \frac{1}{d} \frac{\sum_{n\mathbf{k}} \tau_{\mathbf{k}} |v^n_{\mathbf{k}}|^2 e^{-E^n_{\mathbf{k}}/k_B T}}{\sum_{\mathbf{k}} e^{-E^n_{\mathbf{k}}/k_B T}} \tag{4.16}$$

or simply, in our case, as

$$D = \frac{\hbar}{2} \sum_{\mathbf{k},n} \frac{|v^n_{\mathbf{k}}|^2}{\Gamma^n_{\mathbf{k}}} \frac{f^n_{\mathbf{k}}}{\mathcal{Z}} \quad , \tag{4.17}$$

with a thermalized Boltzmann distribution $f^n_{\mathbf{k}} \propto e^{-E^n_{\mathbf{k}}/k_B T}$ in the low-density limit $\mathcal{Z}$ the partition function, and $\Gamma^n_{\mathbf{k}} = \hbar \tau^{-1}_{\mathbf{k}}$ the polariton scattering rates via phonon interaction. Note that this approximation can generally lead to an overestimation of the actual occupation of quasi-photonic polariton states in the upper polariton branch. However, in the considered regime of resonant exciton and cavity energies, not too high temperatures and relatively large Rabi splittings, these effects are found to be small.

The many-particle mechanisms behind the diffusion can differ considerably when moving from TMD monolayers to TMD bulk materials. In the monolayer case, the reduced screening leads to large excitonic binding energies. As a consequence, diffusion is typically dominated by excitons. Nevertheless, contributions from the faster diffusing electron-hole plasma can still appear for substrates with a large dielectric constant, as observed for hBN-encapsulated TMDs at higher temperatures [105]. Bulk materials are expected to have smaller excitonic effects and thus higher diffusion coefficients in the range of 10 cm^2/s, as observed e.g. for MoS_2 [100] and $MoTe_2$ [106].

4.2 Polariton Diffusion Results

According to Eq. (4.17), the crucial quantities determining the polariton diffusion are the polariton group velocity $v^i_{\mathbf{Q}}$ (see chapter 2), the polariton-phonon scattering rate $\Gamma^i_{\mathbf{Q}}$ (see chapter 3) and the occupation of polariton states $f^i_{\mathbf{Q}}$. Figure 4.1(a) shows the diffusion coefficient as a function of temperature and Rabi splitting. Based on our microscopic approach, we predict polariton diffusion coefficients that are two to three orders of magnitude larger than the ones from the bare exciton. This can be explained by: (i)

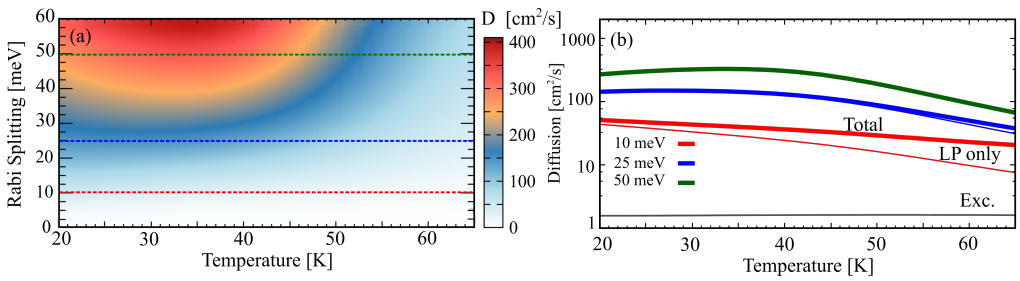

Figure 4.1: (a) Polariton diffusion as a function of temperature and Rabi splitting with (b) cuts evaluated for fixed splittings of 10, 25 and 50 meV. Here, thin lines show the diffusion stemming only from lower polaritons.

the polariton dispersion exhibiting huge group velocities, (ii) effective occupation of fast polaritonic states, and (iii) reduced scattering with phonons of the occupied lower polariton states. These features concern, however, only small-momentum polaritons, while the diffusion coefficients also depend on large-momentum states. The latter is unaffected by points (i) and (iii), as the polariton dispersion and scattering rates correspond to the excitonic values at large momenta (Figs. 2.3, 3.1). Only the relative population remains affected by the presence of lower-lying polariton states at small momenta. As a result, the polariton diffusion coefficient results from a non-trivial interplay between the few very fast states within the light cone and excitonic-like states outside the cone. Interestingly, for $\hbar\Omega_{\mathrm{R}} = 50$ meV, we observe a maximum in the polariton diffusion at around 40K. This can be traced back to the occupation discussed in chapter 2 Fig. 2.4: At 40 K, fast polariton states with a maximum group velocity at approximately $Q \lesssim 1.3\mu\mathrm{m}^{-1}$ are efficiently populated resulting in a maximum diffusion. Further increasing the temperature occupies states at higher momenta (and a smaller group velocity), inducing a decrease of D.

In Fig. 4.1(b), we show the temperature dependence of the polariton diffusion coefficient at three fixed values for the Rabi splitting in comparison with the excitonic value (thin grey line). For increasing temperature, the polariton diffusion decreases towards the bare exciton diffusion (with D in the range of a few cm^2/s) and this occurs faster for smaller Rabi splittings $\hbar\Omega_{\mathrm{R}}$. At higher temperatures, the amount of occupied slower quasi-excitonic states outside the light cone becomes larger. Comparing the total diffusion coefficient with the contribution stemming only from the lower polariton states (thin lines),

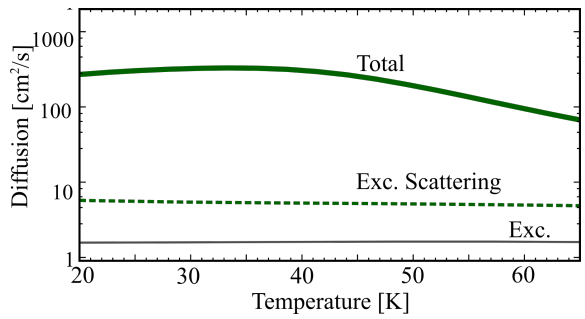

Figure 4.2: Polariton diffusion assuming exciton-phonon scattering rates illustrating the impact of the changed scattering for polaritons.

we find that the LP contribution is dominant for $\hbar\Omega_{\mathrm{R}} = 25$ and 50 meV, as the UP states are only marginally occupied for the considered low temperatures. For the lower Rabi splitting of $\hbar\Omega_{\mathrm{R}}$=10 meV, we find that the total and the LP diffusion start to deviate at higher temperatures indicating the increasing weight of the UP diffusion.

To illustrate the impact of the polariton-phonon scattering on the diffusion, we calculate in a "thought" experiment the polariton diffusion assuming exciton scattering rates, cf. the dashed line in Fig.4.2. We observe a significant decrease in the polariton diffusion by more than one order of magnitude, indicating the important role of polariton-phonon scattering. Note, however, that the polariton diffusion coefficient still remains considerably higher than the exciton one (thin grey line), reflecting the strong impact of the polariton group velocity. Interestingly, the peak at 40 K shown in the full polaritonic case disappears as the excitonic scattering rates decrease the distinction between fast and slow polariton states in view of their weak momentum dependence (Fig. 2.4(a)).

CHAPTER 5

Optical Absorption

The polariton absorption spectrum is especially informative as it unambiguously demonstrates strong coupling via the Rabi splitting.
In this chapter, we introduce Paper II, investigating how the excitons-polariton optical absorption spectra behave and differ for different TMDs.

5.1 Theoretical Background

Cavity polaritons represent an open system that can couple via their photonic part to the outside universe. We can model them using the Heisenberg-Langevin equations along with the input-output relations [72]. Notably, the input-output approach allows us to connect the internal dynamics of the cavity with the external radiation field, which is what is measured in experiments. Therefore, we calculate the equation of motion for polaritons, including the external radiation field and the interaction with phonons. We

consider the situation, where the input laser creates a coherent population of polaritons. The starting point is the Heisenberg equations of motion for the coherent population of polariton and external radiation field. For this, we make a correlation expansion including the dynamics of the phonon-assisted polarization. The derivation of the polariton equations of motions is found in chapter 2, where the polariton dynamics in Fourier space are determined by equation (2.32). Now, we consider the full-time-reversed system to derive the input-output relations. The photon reservoir dynamics is now solved in terms of the output fields [62]. Furthermore, the dynamics of the polariton recombination must be solved in terms of a future time. For simplicity, we consider only restricted-time reversal [107] (i.e. loss remains as loss and does not transform into gain); hence, the input-output relations can be shown not to be impacted by the presence of phonons in the system, thus let us start from equation (2.31)

$$i\hbar\frac{d}{dt}\hat{Y}^n_{\mathbf{k}}(t) = (E^i_{\mathbf{k}} - i\hbar\Gamma^n_{\mathbf{k}})\hat{Y}^n_{\mathbf{k}}(t) - i\hbar\sum_{n'}[h^{n,*}_{\mathrm{c},\mathbf{k}}h^{n'}_{\mathrm{c},\mathbf{k}}(\kappa_{\mathrm{L},\mathbf{k}} + \kappa_{\mathrm{R},\mathbf{k}})]\hat{Y}^{n'}_{\mathbf{k}}(t) + i\hbar h^{n,*}_{\mathrm{c},\mathbf{k}}\sqrt{2\kappa_{\mathrm{L},\mathbf{k}}}b_{3,\mathbf{k}}(t) - i\hbar h^{n,*}_{\mathrm{c},\mathbf{k}}\sqrt{2\kappa_{\mathrm{R},\mathbf{k}}}b_{4,\mathbf{k}}(t) \tag{5.1}$$

to give

$$h^{n,*}_{\mathrm{c},\mathbf{k}}\sqrt{2\kappa_{\mathrm{L},\mathbf{k}}}b_{1,\mathbf{k}}(t) - h^{n,*}_{\mathrm{c},\mathbf{k}}\sqrt{2\kappa_{\mathrm{R},\mathbf{k}}}b_{2,\mathbf{k}}(t) = \sum_{n'}\left[h^{n,*}_{\mathrm{c},\mathbf{k}}h^{n'}_{\mathrm{c},\mathbf{k}}(\kappa_{\mathrm{L},\mathbf{k}} + \kappa_{\mathrm{R},\mathbf{k}})\right]\hat{Y}^{n'}_{\mathbf{k}}(t) + h^{n,*}_{\mathrm{c},\mathbf{k}}\sqrt{2\kappa_{\mathrm{L},\mathbf{k}}}\sum_{n'}h^{n'}_{\mathrm{c},\mathbf{k}}\hat{Y}^{n'}_{\mathbf{k}}(t) - b_{4,\mathbf{k}}(t) \tag{5.2}$$

with the output fields

$$b_{3,\mathbf{k}}(t) = -\int_{-\infty}^{\infty}\frac{d\omega}{2\pi}\hat{\mathcal{B}}_{\mathrm{R}\mathbf{k}\omega}(t_1)e^{-i\omega(t-t_1)}, \tag{5.3}$$

$$b_{4,\mathbf{k}}(t) = +\int_{-\infty}^{\infty}\frac{d\omega}{2\pi}\hat{\mathcal{B}}_{\mathrm{L}\mathbf{k}\omega}(t_1)e^{-i\omega(t-t_1)}. \tag{5.4}$$

To better visualise the input and output fields $b_{i,\mathbf{k}}(t)$ in figure 5.1 we have a schematic representation to show the roles of the four fields. The input-output relations are found by switching off each port in turn:

$$\kappa_{\mathrm{R},\mathbf{k}} = 0: \qquad b_{1,\mathbf{k}}(t) = \sqrt{2\kappa_{\mathrm{L},\mathbf{k}}}\sum_{n'}h^{n'}_{\mathrm{c},\mathbf{k}}\hat{Y}^{n'}_{\mathbf{k}}(t) - b_{4,\mathbf{k}}(t), \tag{5.5}$$

$$\kappa_{\mathrm{L},\mathbf{k}} = 0: \qquad b_{2,\mathbf{k}}(t) = \sqrt{2\kappa_{\mathrm{R},\mathbf{k}}}\sum_{n'}h^{n'}_{\mathrm{c},\mathbf{k}}\hat{Y}^{n'}_{\mathbf{k}}(t) - b_{3,\mathbf{k}}(t). \tag{5.6}$$

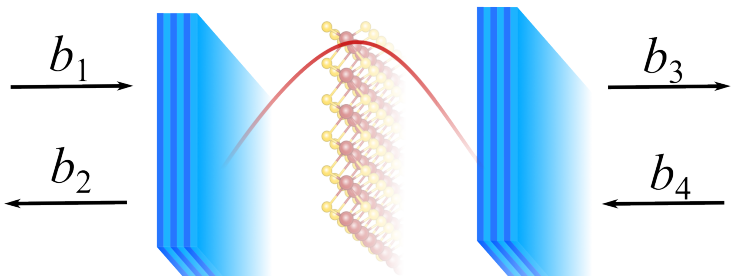

Figure 5.1: Schematic representation of the input and output fields $b_{i,\mathbf{k}}(t)$ in the system.

Then, we Fourier transform these equations and use Eq. (2.32). Let us calculate the transmission, with $b_2 = 0$

$$it^n_{\mathbf{k}}(\omega) = \frac{b_{3,\mathbf{k}}(\omega)}{b_{1,\mathbf{k}}(\omega)} = -\frac{\Omega_{\mathbf{k}}(\omega)\sqrt{2\kappa_{\mathrm{R},\mathbf{k}}}\sqrt{2\kappa_{\mathrm{L},\mathbf{k}}}}{1+\Omega_{\mathbf{k}}(\omega)[\sqrt{2\kappa_{\mathrm{L},\mathbf{k}}}+\sqrt{2\kappa_{\mathrm{R},\mathbf{k}}}]}, \tag{5.7}$$

with

$$\Omega_{\mathbf{k}}(\omega) = \sum_n \frac{|h^n_{\mathrm{c},\mathbf{k}}|^2}{i(\omega^n_{\mathbf{k}} - \omega + \Gamma^n_{\mathbf{k}})}. \tag{5.8}$$

Similarly for reflection:

$$r^n_{\mathbf{k}}(\omega) = \frac{b_{4,\mathbf{k}}}{b_{1,\mathbf{k}}} = \frac{-1+\Omega_{\mathbf{k}}(\omega)[\kappa_{\mathrm{L},\mathbf{k}} - \kappa_{\mathrm{R},\mathbf{k}}]}{1+\Omega_{\mathbf{k}}(\omega)[\kappa_{\mathrm{L},\mathbf{k}} + \kappa_{\mathrm{R},\mathbf{k}}]}. \tag{5.9}$$

In the end, we can simply use the transmission and reflection coefficient assuming the case of a single polariton and for a symmetric cavity $\kappa_L = \kappa_R$:

$$it^n_{\mathbf{k}}(\hbar\omega) = -\frac{2\gamma^n_{\mathbf{k}}}{i(E^n_{\mathbf{k}} - \hbar\omega) + \Gamma^n_{\mathbf{k}} + 2\gamma^n_{\mathbf{k}}}, \qquad r^n_{\mathbf{k}}(\hbar\omega) = \frac{i(E^n_{\mathbf{k}} - \hbar\omega) + \Gamma^n_{\mathbf{k}}}{i(E^n_{\mathbf{k}} - \hbar\omega) + \Gamma^n_{\mathbf{k}} + 2\gamma^n_{\mathbf{k}}}, \tag{5.10}$$

with $\gamma^n_{\mathbf{k}}$ as the effective cavity decay rate. Here, we have neglected interference effects between polaritons. Finally, we obtain an Elliot-like formula for the polariton absorption [62]

$$A^n_{\mathbf{k}}(\hbar\omega) = 1 - |r^n_{\mathbf{k}}(\hbar\omega)|^2 - |it^n_{\mathbf{k}}(\hbar\omega)|^2 = \frac{4\gamma^n_{\mathbf{k}}\Gamma^n_{\mathbf{k}}}{(E^n_{\mathbf{k}} - \hbar\omega)^2 + (2\gamma^n_{\mathbf{k}} + \Gamma^n_{\mathbf{k}})^2}, \tag{5.11}$$

for each polariton branch and momentum $n, \mathbf{k}$. The obtained equation is similar to the expression found in Ref. [62]. However, the key difference lies in the microscopic treatment of polariton-phonon interaction. This means that phonons can change the momentum of the excitonic component of the polariton, leading to a momentum-dependent scattering rate. In Eq. (5.11) we introduced the decay rates

$$\gamma^n_{\mathbf{k}} = \hbar c(1 - |r_m|^2)|h_{\mathrm{c},\mathbf{k}}|^2/(4L_{cav}), \tag{5.12}$$

$$\Gamma^n_{\mathbf{k}} = 2\pi \sum_{n'\alpha\mathbf{k}'} |\tilde{\mathcal{D}}^{n'n}_{\alpha,\mathbf{k}'-\mathbf{k}}|^2 \left(\frac{1}{2} \pm \frac{1}{2} + n^b_{\alpha,\mathbf{k}'-\mathbf{k}}\right) \times$$
$$\times L_{\tilde{\gamma}_0}\left(E^{n'}_{\mathbf{k}'} - E^n_{\mathbf{k}} \pm E^b_{\alpha,\mathbf{k}'-\mathbf{k}}\right), \tag{5.13}$$

where $\gamma^n_{\mathbf{k}}$ is the effective cavity decay rate of one port and $\Gamma^n_{\mathbf{k}}$ is the polariton-phonon scattering rate. Here we are summing over all possible scattering channels from a polariton $n, \mathbf{k}$ to all possible receiving polaritons $n', \mathbf{k}'$ via interaction with a phonon with mode α and momentum $\mathbf{q}$, such that the overall momentum is conserved. The quality factor of the cavity reads $Q_f = E^{\mathrm{c}}_0 L_{cav}/[\hbar c(1 - |r_m|^2)|)]$, where r_m is the reflectivity of the cavity. In this work, if not stated otherwise, we use the default value of $r_m = 0.99$. Crucially, the polaritonic Elliot formula offers insight into how underlying microscopic decay channels manifest in the absorption of light by polaritons, which would not be possible using the more commonly used classical transfer-matrix method [4]. Evaluating Eq. (5.11) at resonance reveals that absorption is maximized when the two effective polariton decay rates are closest in value. It follows that maximum absorption of 0.5 is possible at the so-called critical coupling condition [108, 109] of $2\gamma^n_{\mathbf{k}} = \Gamma^n_{\mathbf{k}}$, i.e. when the leakage out of both ports of the cavity is equal to the exciton dissipation rate within the TMD layer in the cavity. The maximum possible absorption of 50% is a well-known constraint for mirror-symmetric two-port systems that support a single resonance [110, 111]. We expect the presence of dark excitons to significantly increase the polariton-phonon scattering rates in tungsten-based TMDs (as there they are the energetically lowest states). The opening of intervalley scattering channels is expected to strongly impact the balance between the effective radiative coupling and scattering loss, which should translate into measurable signatures in polariton absorption spectra.

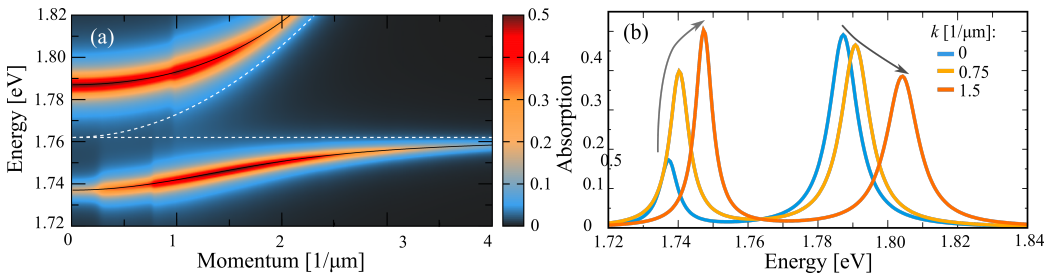

Figure 5.2: Polariton absorption. (a) Surface plot of absorption in an hBN-encapsulated WSe_2 monolayer as a function of momentum and energy at a temperature of 77 K, assuming a Rabi splitting of $\hbar\Omega_R = 50$ meV and a cavity quality factor of Q_f=160. The dashed white lines correspond to the bare exciton and cavity dispersion, while the solid black lines describe the polariton dispersion. (b) Absorption cuts as a function of energy for three different momenta.

5.2 Polariton Absorption of WSe_2

First, we evaluate Eq. (5.11), using numerically calculated polariton-phonon scattering rates from chapter 3, to study the polariton absorption in the strong-coupling regime for an hBN-encapsulated WSe_2 monolayer integrated into a Fabry-Perot cavity with a quality factor of $Q_f \approx 160$ and a Rabi splitting of $\hbar\Omega_R = 50$ meV. Figure 5.2(a) presents an energy- and in-plane momentum-resolved surface plot of the polariton absorption. Interestingly, we find the upper polariton to be much higher in intensity than the lower polariton at $k = 0$ μm^{-1} (cf. also the blue lines in Fig.5.2(b)). Previous reports in GaAs have shown that in the case of zero detuning (also called resonant case), the lower and upper polariton peak intensities are similar [112, 113]. In the resonant case, the two polaritons have an equal photonic and excitonic contribution at $k = 0$. Hence, the cavity decay rate, $\gamma^n_{\mathbf{k}}$, is the same for both polaritons. As a result, the phonon-induced decay rate of polaritons must be responsible for the observed difference in the height of absorption peaks. Furthermore, we find that the absorption is enhanced for increasing momenta for the lower polariton (A^{LP}) up to approximately $k = 1.6$ μm^{-1}, while it is reduced for the upper polariton (A^{UP}), (cf. also the absorption cuts in Fig. 5.2(b)). Moreover, we observe that not only the absorption intensity but also the linewidth of A^{LP} becomes larger for increasing in-plane momentum before it is again reduced for momenta higher

than $k = 1.6\ \mu\text{m}^{-1}$. The absorption intensity and the spectral linewidth of polariton resonances can be ascribed to the interplay of the cavity decay and non-radiative decay of polaritons via scattering with phonons.

5.3 Critical Coupling

To explain the different behaviours in the absorption spectra of the upper and lower polariton branch, we plot the maximal absorption $A^n_{\mathbf{k}}$ for UP and LP branch at 77 K in Fig. 5.3(a). The absorption intensity of the UP branch generally decreases with the momentum, however, there is one exception at approximately $k = 1\ \mu\text{m}^{-1}$, where we observe a small increase (blue line). In contrast, we find an enhanced absorption for the lower polariton branch until approximately $k = 1.6\ \mu\text{m}^{-1}$ where it achieves the maximum value of $A = 0.5$ (red line). The resonant absorption also includes several steep step-like enhancements until the maximum is reached. To better understand the change of the absorption as a function of the in-plane momentum and the opposite behaviour of the upper and the lower polariton branch observed in Fig. 5.3(a), we investigate in Fig. 5.3(b) the momentum-dependent cavity decay rate $\gamma^n_{\mathbf{k}}$ and polariton-phonon scattering rate $\Gamma^n_{\mathbf{k}}$, cf. Eqs. (5.12) and (5.13). We find that for the lower polariton branch, the critical coupling condition of $\Gamma^n_{\mathbf{k}} = 2\gamma^n_{\mathbf{k}}$ is reached at $k = 1.6\ \mu\text{m}^{-1}$, as denoted with the black vertical line in Fig. 5.3(b). This corresponds exactly to the momentum where the maximal absorption of $A^{LP} = 0.5$ is reached. The microscopic calculation of polariton-photon scattering rates explains the step-like increase in the absorption of both the UP and LP polariton branch. These can be clearly attributed to an increase of the polariton-phonon scattering rates at certain momenta (at $k \approx 0.3$, 0.8, 2.4 and 3.1 μm^{-1} for $\Gamma^{LP}_{\mathbf{k}}$ and at 1 μm^{-1} for $\Gamma^{UP}_{\mathbf{k}}$). Importantly, each of the steep increases for the LP absorption/rates is a signature of an opening of an intervalley scattering channel into dark exciton states. In Fig. 5.3(c), we plot the lower polariton dispersion in relation to the bright exciton energy together with the phonon dispersion for LA, TA and TO modes that are responsible for the scattering into the dark KΛ excitons. For a more detailed description of the step-like behaviour of the lower polariton, see chapter 3. We point that the cavity decay rate $\gamma^n_{\mathbf{k}}$ increases/decreases smoothly with k for the UP/LP branch, cf. the dashed

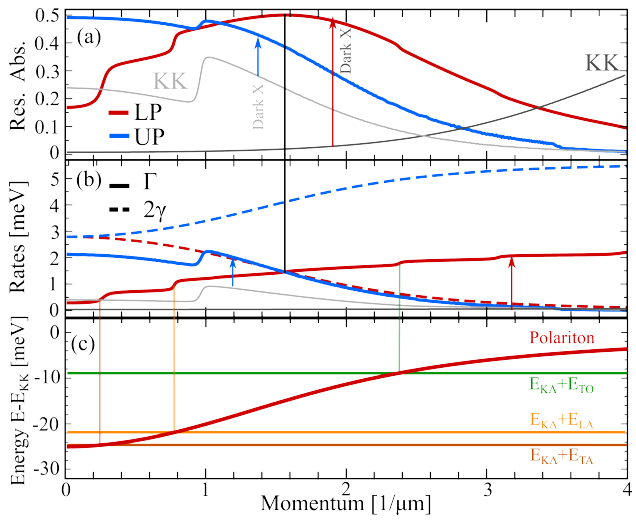

Figure 5.3: Critical coupling. (a) Maximal absorption at the resonant energy as a function of momentum for the lower (red, LP) and upper (blue, UP) polariton at 77 K and $\hbar\Omega_R = 50$ meV, $Q_f \approx$160. (b) Polariton-phonon scattering rate $\Gamma^n_{\mathbf{k}}$ (solid lines) and cavity decay rate $\gamma^n_{\mathbf{k}}$ (dashed lines) as a function of momentum for the upper and lower polariton (same colours as in (a)). The maximum value of absorption of $An = 0.5$ identifies the critical coupling conditions $\Gamma^n_{\mathbf{k}} = 2\gamma^n_{\mathbf{k}}$ for the respective polariton and it is marked by a vertical black line. The grey lines show the case without considering dark states and only taking into account the bright KK excitons. (c) Lower polariton dispersion (red line) and phonon energies (plus the energy of the dark KΛ exciton) showing the opening of emission channels into the dark exciton states at $k \approx 0.3$, 0.8, 2.4 and μm^{-1}.

lines in Fig. 5.3(b). This increase/decrease is determined by the photonic Hopfield coefficient, which increases for the UP and decreases for the LP branch.

To illustrate the importance of dark excitons, we also show the polariton absorption and the polariton-phonon scattering rates without including dark exciton states, i.e. we only take into account the bright KK excitons (grey lines in Figs. 5.3(a,b)). We find that for the lower polariton the resonant absorption is drastically reduced at small momenta, with the critical coupling condition shifted to higher momenta. We also find that the steep increases step-like increases found for these polaritons disappear (red vs. lower grey line), as they stem from scattering into dark excitons.

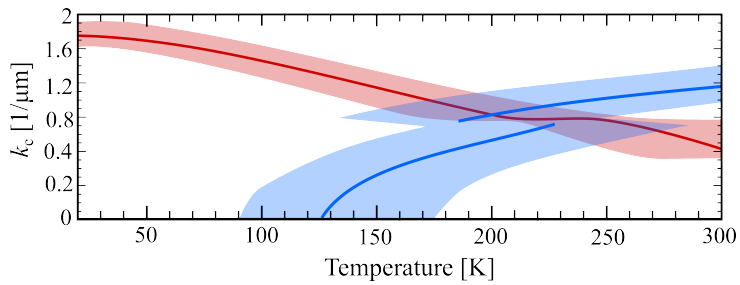

Figure 5.4: Critical coupling momentum k_c as a function of temperature for the upper (blue) and lower polariton (red). The shaded area corresponds to the range $0.5 \geq A^n \geq 0.495$.

So far, we have only considered the polariton absorption at 77K, where the critical coupling condition can only be reached for the lower polariton branch. To further investigate this, we present in Fig. 5.4 the critical coupling momentum k_c as a function of temperature for the upper (blue line) and the lower polariton (red line). The blue- and red-shaded areas correspond to the region $0.5 \geq A^n \geq 0.495$ to take into account uncertainties in the experimental measurement of the maximal absorption. As we increase the temperature, the critical coupling occurs at smaller momenta for the LP branch due to increased scattering with phonons. Since the cavity decay rates $\gamma^i_{\mathbf{k}}$ are temperature-independent within our model, the overall increase in $\Gamma^n_{\mathbf{k}}$ at higher temperatures results in smaller k_c fulfilling the critical coupling conditions. Interestingly, for the UP branch, we find that there is no critical coupling for temperatures below approximately 125K. We show in Fig. 5.3(b) that at $k = 0$ the cavity decay rate $\gamma^n_{\mathbf{k}}$ is larger than $\Gamma^n_{\mathbf{k}}$. However, while $\gamma^{LP}_{\mathbf{k}}$ decreases for increasing momenta, thus approaching the smaller values of $\Gamma^n_{\mathbf{k}}$, the opposite takes place for $\gamma^{UP}_{\mathbf{k}}$. Thus, for upper polaritons, the critical coupling can only occur at higher temperatures, where $\Gamma^n_{\mathbf{k}}$ is considerably enhanced. Interestingly, we find that at around 200K two different momenta fulfil the critical coupling condition for UP (blue lines in Fig. 5.4). At these temperatures, the cavity decay rate crosses the polariton-phonon scattering rate in the region of the opening of the optical emission (step-like increase), where we can have the same value of scattering and cavity-decay rates for two (or more) momenta.

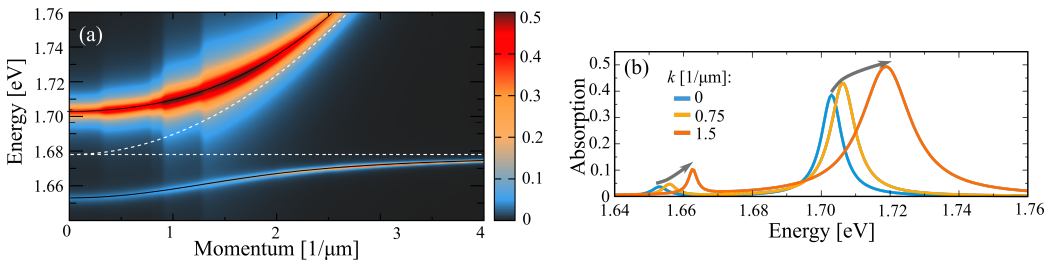

Figure 5.5: Absorption of $MoSe_2$. (a) Surface plot of polariton absorption of an hBN-encapsulated $MoSe_2$ monolayer as a function of momentum and energy (77K, $\hbar\Omega_R = 50$ meV and $Q_f \approx$160) and (b) Absorption cuts as a function of energy for three different momenta.

5.4 Polariton Absorption of $MoSe_2$

So far we have studied the polariton absorption for WSe_2 monolayers, where dark excitons turned out to play a crucial role. Now we investigate the $MoSe_2$ monolayer exhibiting a different energetic alignment of dark and bright states. With the latter being the lowest ones in $MoSe_2$ [3, 41, 69], we expect only a negligible contribution from dark excitons.

Similarly to the case of WSe_2, we show in Fig. 5.5(a) the absorption of polaritons as a function of momentum and energy for the zero-detuning case at T =77 K. We find a drastic reduction in absorption as well as in the linewidth of the LP absorption compared to WSe_2 (Fig. 5.2(a)). This can be clearly observed in the momentum cuts shown in Fig. 5.5(b). Although the intensity of the resonant absorption increases for larger momenta, similar to the case of WSe_2, quantitatively the increase is much slower, reaching only a maximal value of approximately 0.1 at $k = 1.5\mu\text{m}^{-1}$ (compared to almost 0.5 predicted for WSe_2). Interestingly, for larger momenta, we also find an increase of the absorption for the UP branch (Fig. 5.5(b)) - opposite to the case of WSe_2 (Fig. 5.5(b)). In addition, we observe a large increase in the spectral width of polariton resonances at larger in-plane momenta k.

To microscopically understand the qualitative as well as quantitative differences of the momentum-resolved absorption in $MoSe_2$ and WSe_2, we investigate the intensity of the resonant polariton absorption and the underlying polariton-phonon and cavity decay rates. We assume the same value of reflectivity $r_m = 0.99$ as in Fig. 5.3, resulting in similar cavity decay rates $\gamma^n_{\mathbf{k}}$ as for WSe_2. We show both the absorption and decay rates also for the case

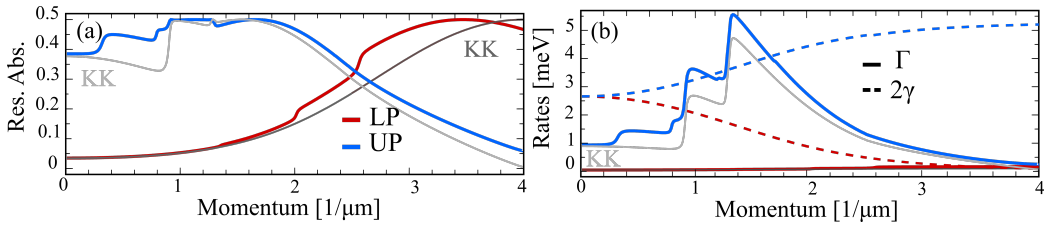

Figure 5.6: Absorption of $MoSe_2$. (a) Absorption intensity as a function of momentum for the lower (LP) and the upper (UP) polariton branch. (b) Decay rates $\Gamma^n_{\mathbf{k}}$ and $2\gamma^n_{\mathbf{k}}$ as a function of momentum for the LP and UP branches. The thin grey lines in (a) and (b) correspond to the case without dark excitons (considering only the bright KK excitons).

without dark excitons (grey lines in Figs. 5.6(a,b)). As expected, in $MoSe_2$ there is only a minor contribution of dark states (as we previously saw in the scattering rates, see chapter 3). Nevertheless, the decrease of the cavity decay rate $\gamma^n_{\mathbf{k}}$ with increasing momenta allows for the critical coupling condition at the very high momenta of $k_c = 3.25\ \mu\text{m}^{-1}$ (cf. Fig. 5.6(b)), where the LP absorption reaches its maximum value of $A^n = 0.5$ (Fig. 5.6(a)). Interestingly, even though dark excitons have only a small contribution, their presence shifts the critical coupling condition to a smaller momentum (cf. grey vs red line in Fig. 5.6(a)). For the upper polariton, the intra-valley scattering contribution is the dominant (only small deviations between the grey and blue line). In contrast to WSe_2, we observe a large increase in the phonon-scattering rates for the UP branch, reflecting a more efficient intravalley scattering with optical modes in $MoSe_2$ [83]. This leads to the much broader spectral width of the resonances observed in Fig. 5.5(b). The contribution of dark excitons is minor, however, we still observe an opening of an emission channel into dark states, cf. the step-like increase of $\Gamma^{UP}_{\mathbf{k}}$ at $k \approx 0.4\ \mu\text{m}^{-1}$. This opening is important for understanding the increase of the resonant absorption when going from $k = 0$ to $k = 0.75\ \mu\text{m}^{-1}$ observed in Fig. 5.5(b) (in contrast to the prediction for WSe_2 in Fig. 5.2(a)). Without dark states, there would be a decrease of the absorption up to approximately $0.9\ \mu\text{m}^{-1}$ (cf. the grey line in Fig. 5.6(a)). In $MoSe_2$, the upper polariton fulfils the critical coupling condition at the four different momenta $k_c \approx 1$, 1.2, 1.3 and 1.6 $1/\mu$m. The lowest two are a consequence of polariton scattering into dark exciton states.

CHAPTER 6

Conclusion and Outlook

In this thesis, we have provided a microscopic description of transport and optics of exciton-polaritons in atomically thin semiconductors. The theoretical approach presented here is based on the density matrix formalism combined with the Hopfield approach. In particular, we used our model to study the polariton diffusion coefficient in an hBN-encapsulated $MoSe_2$ monolayer. To calculate the polariton absorption coefficient we used the Heisenberg-Langevin equations, together with the input-output formalism. Our work provides insight into (1) accelerated polariton diffusion, which opens the door to ballistic polariton propagation, and (2) the impact of dark excitons on optical absorption, potentially suggesting experiments that could determine the energy of these dark exciton states.

So far, we consider the case where the energy of the cavity was in resonance with the energy of the exciton. However, recent experiments have shown that we can use detuning to make the lower polariton the lowest energetic state of WSe_2 monolayers, and, consequently brighten the dark material [114]. In the second part of my PhD, we want to study how detuning affects the

polariton absorption for the tungsten-based material as we predict a decrease in the absorption of the lower polariton with an increased negative detuning. Furthermore, we mentioned that the change in the polariton dispersions has effects on the optics, transports and dynamics properties of the material. While we have performed studies on optics and transport so far, we will focus on exciton-polaritons and temporally resolve the polariton physics in 2D materials.

Acknowledgments

First of all, I would like to thank my supervisor, Ermin Malic, for his consistent support, guidance and encouragement. I would also like to thank Roberto Rosati for his endless patience towards my numerous questions and for his contagious enthusiasm and encouragement.

Further, I thank my examiner, Jari Kinaret, for carefully reading and for the useful comments on my thesis and Thilo Bauch for taking the time for being my opponent.

I could not forget to thank all the members of the Ultrafast Quantum Dynamics group in Marburg and Chalmers, especially Jamie Fitzgerald for all the interesting conversations on polaritons, but also Raul, Daniel and Joakim for the coffee and lunch breaks.

Finally, a big thanks to my family and friends in Portugal. It does not matter if there are so many kilometres separating us, you keep supporting and helping me in every way you can, through the good and bad days. To my boyfriend, I only say 143.

Bibliography

[1] PJ Dean, B Fischer, DC Herbert, J Lagois, and PY Yu. *Excitons*, volume 14. Springer Science & Business Media, 2012.

[2] Raul Perea-Causin, Daniel Erkensten, Jamie M Fitzgerald, Joshua JP Thompson, Roberto Rosati, Samuel Brem, and Ermin Malic. Exciton optics, dynamics, and transport in atomically thin semiconductors. *APL Materials*, 10(10):100701, 2022.

[3] Thomas Mueller and Ermin Malic. Exciton physics and device application of two-dimensional transition metal dichalcogenide semiconductors. *NPJ 2D Mater. Appl*, 2(1):29, Sep 2018.

[4] Alexey V Kavokin, Jeremy J Baumberg, Guillaume Malpuech, and Fabrice P Laussy. *Microcavities*, volume 21. Oxford university press, 2017.

[5] Obafunso A Ajayi, Jenny V Ardelean, Gabriella D Shepard, Jue Wang, Abhinandan Antony, Takeshi Taniguchi, Kenji Watanabe, Tony F Heinz, Stefan Strauf, X-Y Zhu, and James C Hone. On the influence of reabsorption on the decay of fluorescence in molecular crystals. *Optika i Spectr.*, 3(3):84, 1957.

[6] JJ Hopfield. Theory of the contribution of excitons to the complex dielectric constant of crystals. *Phys. Rev.*, 112(5):1555, 1958.

[7] DL Mills and E Burstein. Polaritons: the electromagnetic modes of media. *Reports on Progress in Physics*, 37(7):817, 1974.

[8] JM Pitarke, VM Silkin, EV Chulkov, and PM Echenique. Theory of surface plasmons and surface-plasmon polaritons. *Rep. Prog. Phys*, 70(1):1, 2006.

[9] Zubin Jacob. Hyperbolic phonon–polaritons. *Nature Mat.*, 13(12):1081–1083, 2014.

[10] Dengke Zhang, Xiao-Qing Luo, Yi-Pu Wang, Tie-Fu Li, and JQ You. Observation of the exceptional point in cavity magnon-polaritons. *Nature communications*, 8(1):1–6, 2017.

[11] Mark Steger, Gangqiang Liu, Bryan Nelsen, Chitra Gautham, David W Snoke, Ryan Balili, Loren Pfeiffer, and Ken West. Long-range ballistic motion and coherent flow of long-lifetime polaritons. *Phys. Rev. B*, 88(23):235314, 2013.

[12] J Vondran, F Spitzer, M Bayer, IA Akimov, A Trautmann, M Reichelt, C Meier, N Weber, T Meier, R André, et al. Spatially asymmetric transients of propagating exciton-polariton modes in a planar CdZnTe/CdMgTe guiding structure. *Phys. Rev. B*, 100(15):155308, 2019.

[13] M. Wurdack, E. Estrecho, S. Todd, T. Yun, M. Pieczarka, S. K. Earl, J. A. Davis, C. Schneider, A. G. Truscott, and E. A. Ostrovskaya. Motional narrowing, ballistic transport, and trapping of room-temperature exciton–polaritons in an atomically-thin semiconductor. *Nat. Commun.*, 12(1):5366, Sep 2021.

[14] EL Ivchenko. Spatial dispersion effects in the exciton resonance region, 1982.

[15] VA Kosobukin, RP Seisyan, and SA Vaganov. Exciton-polariton light absorption in bulk GaAs and semiconductor superlattices. *Semicond. Sci. tech.*, 8(7):1235, 1993.

[16] D Fröhlich, A Kulik, B Uebbing, A Mysyrowicz, V Langer, H Stolz, and W Von der Osten. Coherent propagation and quantum beats of quadrupole polaritons in Cu_2O. *Phys. Rev. Lett.*, 67(17):2343, 1991.

[17] Giovanna Panzarini and Lucio Claudio Andreani. Bulk polariton beatings and two-dimensional radiative decay: Analysis of time-resolved transmission through a dispersive film. *Solid State Commun.*, 102(7):505–509, 1997.

[18] Lucio Claudio Andreani, Francesco Tassone, and Franco Bassani. Radiative lifetime of free excitons in quantum wells. *Solid State Commun.*, 77(9):641–645, 1991.

[19] EL Ivchenko. Excitonic polaritons in periodic quantum-well structures. *Soviet physics. Solid state*, 33(8):1344–1346, 1991.

[20] Alexey Kavokin and Guillaume Malpuech. *Thin Films and Nanostructures: Cavity polaritons*. Elsevier, 2003.

[21] Hui Deng, Hartmut Haug, and Yoshihisa Yamamoto. Exciton-polariton Bose-Einstein condensation. *Rev. Mod. Phys.*, 82(2):1489, 2010.

[22] Claude Weisbuch, Mr Nishioka, A Ishikawa, and Y Arakawa. Observation of the coupled exciton-photon mode splitting in a semiconductor quantum microcavity. *Phys. Rev. Lett.*, 69(23):3314, 1992.

[23] R Houdré, C Weisbuch, RP Stanley, U Oesterle, P Pellandini, and M Ilegems. Measurement of cavity-polariton dispersion curve from angle-resolved photoluminescence experiments. *Phys. Rev. Lett.*, 73(15):2043, 1994.

[24] F Jahnke, M Kira, SW Koch, G Khitrova, EK Lindmark, TR Nelson Jr, DV Wick, JD Berger, O Lyngnes, HM Gibbs, et al. Excitonic nonlinearities of semiconductor microcavities in the nonperturbative regime. *Phys. Rev. Lett.*, 77(26):5257, 1996.

[25] Wolfgang Langbein and Jørn M Hvam. Elastic scattering dynamics of cavity polaritons: Evidence for time-energy uncertainty and polariton localization. *Phys. Rev. Lett.*, 88(4):047401, 2002.

[26] DG Lidzey, AM Fox, MD Rahn, MS Skolnick, VM Agranovich, and S Walker. Experimental study of light emission from strongly coupled organic semiconductor microcavities following nonresonant laser excitation. *Phys. Rev. B*, 65(19):195312, 2002.

[27] Xiaoze Liu, Tal Galfsky, Zheng Sun, Fengnian Xia, Erh-chen Lin, Yi-Hsien Lee, Stéphane Kéna-Cohen, and Vinod M Menon. Strong light–matter coupling in two-dimensional atomic crystals. *Nat. Photon.*, 9(1):30–34, 2015.

[28] S Dufferwiel, S Schwarz, F Withers, AAP Trichet, F Li, M Sich, O Del Pozo-Zamudio, C Clark, A Nalitov, DD Solnyshkov, et al. Exciton–polaritons in Van der Waals heterostructures embedded in tunable microcavities. *Nat. Commun.*, 6(1):1–7, 2015.

[29] Christian Schneider, Mikhail M Glazov, Tobias Korn, Sven Höfling, and Bernhard Urbaszek. Two-dimensional semiconductors in the regime of strong light-matter coupling. *Nat. Commun.*, 9(1):1–9, 2018.

[30] Jacek Kasprzak, Murielle Richard, S Kundermann, A Baas, P Jeambrun, Jonathan Mark James Keeling, FM Marchetti, MH Szymańska, R André, JL Staehli, et al. Bose–Einstein condensation of exciton polaritons. *Nature*, 443(7110):409–414, 2006.

[31] Xuekai Ma, Bernd Berger, Marc Aßmann, Rodislav Driben, Torsten Meier, Christian Schneider, Sven Höfling, and Stefan Schumacher. Realization of all-optical vortex switching in exciton-polariton condensates. *Nat. Commun.*, 11(1):1–7, 2020.

[32] Carlos Anton-Solanas, Maximilian Waldherr, Martin Klaas, Holger Suchomel, Tristan H Harder, Hui Cai, Evgeny Sedov, Sebastian Klembt, Alexey V Kavokin, Sefaattin Tongay, et al. Bosonic condensation of exciton-polaritons in an atomically thin crystal. *Nat. Mat.*, 20:1233–1239, 2021.

[33] Dario Ballarini, Milena De Giorgi, Emiliano Cancellieri, Romuald Houdré, Elisabeth Giacobino, Roberto Cingolani, Alberto Bramati, Giuseppe Gigli, and Daniele Sanvitto. All-optical polariton transistor. *Nat. Commun.*, 4(1):1–8, 2013.

[34] German V Kolmakov, Leonid M Pomirchi, and Roman Ya Kezerashvili. Toward room-temperature superfluidity of exciton–polaritons in an optical microcavity with an embedded MoS_2 monolayer. *JOSA B*, 33(7):C72–C79, 2016.

[35] S Klembt, TH Harder, OA Egorov, K Winkler, R Ge, MA Bandres, M Emmerling, L Worschech, TCH Liew, M Segev, et al. Exciton-polariton topological insulator. *Nature*, 562(7728):552–556, 2018.

[36] P St-Jean, V Goblot, E Galopin, A Lemaître, T Ozawa, L Le Gratiet, I Sagnes, J Bloch, and A Amo. Lasing in topological edge states of a one-dimensional lattice. *Nat. Photon.*, 11(10):651–656, 2017.

[37] Alberto Amo, TCH Liew, Claire Adrados, Romuald Houdré, Elisabeth Giacobino, AV Kavokin, and A Bramati. Exciton–polariton spin switches. *Nat. Photon.*, 4(6):361–366, 2010.

[38] Sanjib Ghosh and Timothy CH Liew. Quantum computing with exciton-polariton condensates. *Npj Quantum Inf.*, 6(1):1–6, 2020.

[39] Gunnar Berghäuser, Philipp Steinleitner, Philipp Merkl, Rupert Huber, Andreas Knorr, and Ermin Malic. Mapping of the dark exciton landscape in transition metal dichalcogenides. *Phys. Rev. B*, 98:020301, Jul 2018.

[40] Ermin Malic, Malte Selig, Maja Feierabend, Samuel Brem, Dominik Christiansen, Florian Wendler, Andreas Knorr, and Gunnar Berghäuser. Dark excitons in transition metal dichalcogenides. *Phys. Rev. Mater.*, 2:014002, Jan 2018.

[41] Thorsten Deilmann and Kristian Sommer Thygesen. Finite-momentum exciton landscape in mono- and bilayer transition metal dichalcogenides. *2D Mater.*, 6(3):035003, apr 2019.

[42] Koloman Wagner, Jonas Zipfel, Roberto Rosati, Edith Wietek, Jonas D. Ziegler, Samuel Brem, Raül Perea-Causín, Takashi Taniguchi, Kenji Watanabe, Mikhail M. Glazov, Ermin Malic, and Alexey Chernikov. Nonclassical exciton diffusion in monolayer WSe_2. *Phys. Rev. Lett.*, 127:076801, Aug 2021.

[43] Roberto Rosati, Raül Perea-Causín, Samuel Brem, and Ermin Malic. Negative effective excitonic diffusion in monolayer transition metal dichalcogenides. *Nanoscale*, 12:356–363, 2020.

[44] Roberto Rosati, Samuel Brem, Raül Perea-Causín, Robert Schmidt, Iris Niehues, Steffen Michaelis de Vasconcellos, Rudolf Bratschitsch, and Ermin Malic. Strain-dependent exciton diffusion in transition metal dichalcogenides. *2D Materials*, 8(1):015030, 2020.

[45] Roberto Rosati, Koloman Wagner, Samuel Brem, Raül Perea-Causín, Jonas D Ziegler, Jonas Zipfel, Takashi Taniguchi, Kenji Watanabe, Alexey Chernikov, and Ermin Malic. Non-equilibrium diffusion of dark excitons in atomically thin semiconductors. *Nanoscale*, 13(47):19966–19972, 2021.

[46] Marvin Kulig, Jonas Zipfel, Philipp Nagler, Sofia Blanter, Christian Schüller, Tobias Korn, Nicola Paradiso, Mikhail M. Glazov, and Alexey Chernikov. Exciton diffusion and halo effects in monolayer semiconductors. *Phys. Rev. Lett.*, 120:207401, May 2018.

[47] Raül Perea-Causín, Samuel Brem, Roberto Rosati, Roland Jago, Marvin Kulig, Jonas D. Ziegler, Jonas Zipfel, Alexey Chernikov, and Ermin Malic. Exciton propagation and halo formation in two-dimensional materials. *Nano Lett.*, 19(10):7317–7323, Oct 2019.

[48] M. M. Glazov. Phonon wind and drag of excitons in monolayer semiconductors. *Phys. Rev. B*, 100:045426, Jul 2019.

[49] Roberto Rosati, Robert Schmidt, Samuel Brem, Raül Perea-Causín, Iris Niehues, Johannes Kern, Johann A. Preuß, Robert Schneider, Steffen Michaelis de Vasconcellos, Rudolf Bratschitsch, and Ermin Malic. Dark exciton anti-funneling in atomically thin semiconductors. *Nature Commun.*, 12(1):7221, Dec 2021.

[50] Xidong Duan, Chen Wang, Jonathan C. Shaw, Rui Cheng, Yu Chen, Honglai Li, Xueping Wu, Ying Tang, Qinling Zhang, Anlian Pan, Jianhui Jiang, Ruqing Yu, Yu Huang, and Xiangfeng Duan. Lateral epitaxial growth of two-dimensional layered semiconductor heterojunctions. *Nat. Nanotechnol.*, 9(12):1024–1030, Dec 2014.

[51] Yongji Gong, Junhao Lin, Xingli Wang, Gang Shi, Sidong Lei, Zhong Lin, Xiaolong Zou, Gonglan Ye, Robert Vajtai, Boris I. Yakobson, Humberto Terrones, Mauricio Terrones, Beng Kang Tay, Jun Lou, Sokrates T. Pantelides, Zheng Liu, Wu Zhou, and Pulickel M. Ajayan. Vertical and in-plane heterostructures from WS_2/MoS_2 monolayers. *Nat. Mater.*, 13(12):1135–1142, Dec 2014.

[52] Chunming Huang, Sanfeng Wu, Ana M. Sanchez, Jonathan J. P. Peters, Richard Beanland, Jason S. Ross, Pasqual Rivera, Wang Yao, David H. Cobden, and Xiaodong Xu. Lateral heterojunctions within monolayer $MoSe_2$–WSe_2 semiconductors. *Nat. Mater.*, 13(12):1096–1101, Dec 2014.

[53] Ka Wai Lau, Calvin, Zhirui Gong, Hongyi Yu, and Wang Yao. Interface excitons at lateral heterojunctions in monolayer semiconductors. *Phys. Rev. B*, 98:115427, Sep 2018.

[54] Samuel Brem, Kai-Qiang Lin, Roland Gillen, Jonas M Bauer, Janina Maultzsch, John M Lupton, and Ermin Malic. Hybridized intervalley moiré excitons and flat bands in twisted wse_2 bilayers. *Nanoscale*, 12(20):11088–11094, 2020.

[55] Philipp Merkl, Fabian Mooshammer, Samuel Brem, Anna Girnghuber, Kai-Qiang Lin, Leonard Weigl, Marlene Liebich, Chaw-Keong Yong, Roland Gillen, Janina Maultzsch, et al. Twist-tailoring coulomb correlations in van der waals homobilayers. *Nature Commun.*, 11(1):1–7, 2020.

[56] Joakim Hagel, Samuel Brem, Christopher Linderälv, Paul Erhart, and Ermin Malic. Exciton landscape in van der waals heterostructures. *Physical Review Research*, 3(4):043217, 2021.

[57] Daniel Erkensten, Samuel Brem, Koloman Wagner, Roland Gillen, Raül Perea-Causín, Jonas D. Ziegler, Takashi Taniguchi, Kenji Watanabe, Janina Maultzsch, Alexey Chernikov, and Ermin Malic. Dark exciton-exciton annihilation in monolayer WSe_2. *Phys. Rev. B*, 104:L241406, Dec 2021.

[58] Robert Wallauer, Raul Perea-Causin, Lasse Münster, Sarah Zajusch, Samuel Brem, Jens Güdde, Katsumi Tanimura, Kai-Qiang Lin, Rupert

Huber, Ermin Malic, et al. Momentum-resolved observation of exciton formation dynamics in monolayer WS_2. *Nano Lett.*, 21(13):5867–5873, 2021.

[59] Long Yuan, Biyuan Zheng, Qiuchen Zhao, Roman Kempt, Thomas Brumme, Agnieszka Beata Kuc, Chao Ma, Shibin Deng, Anlian Pan, and Libai Huang. Non-equilibrium first-order exciton mott transition at monolayer lateral heterojunctions visualized by ultrafast microscopy. *arXiv preprint arXiv:2111.07887*, 2021.

[60] Dorian Beret, Ioannis Paradisanos, Hassan Lamsaadi, Ziyang Gan, Emad Najafidehaghani, Antony George, Tibor Lehnert, Johannes Biskupek, Ute Kaiser, Shivangi Shree, et al. Exciton spectroscopy and unidirectional transport in mose2-wse2 lateral heterostructures encapsulated in hexagonal boron nitride. *NPJ 2D Mater. Appl*, 6(1):1–8, 2022.

[61] David Schmitt, Jan Philipp Bange, Wiebke Bennecke, AbdulAziz Al-Mutairi, Giuseppe Meneghini, Kenji Watanabe, Takashi Taniguchi, Daniel Steil, D Russell Luke, R Thomas Weitz, et al. Formation of moiré interlayer excitons in space and time. *Nature*, 608(7923):499–503, 2022.

[62] Jamie M Fitzgerald, Joshua JP Thompson, and Ermin Malic. Twist angle tuning of moiré exciton polaritons in van der waals heterostructures. *Nano Lett.*, 22(11):4468–4474, 2022.

[63] G Bley, U Neukirch, and J Gutowski. Exciton polariton diffusion in ZnSe layers. *J. Cryst. Growth*, 184:1095–1099, 1998.

[64] DA Zaitsev, ND Il'ynskaya, AV Koudinov, NK Poletaev, EV Nikitina, A Yu Egorov, AV Kavokin, and RP Seisyan. Diffusive propagation of exciton-polaritons through thin crystal slabs. *Sci. Rep.*, 5(1):11474, 2015.

[65] Malte Selig, Gunnar Berghäuser, Marten Richter, Rudolf Bratschitsch, Andreas Knorr, and Ermin Malic. Dark and bright exciton formation, thermalization, and photoluminescence in monolayer transition metal dichalcogenides. *2D Materials*, 5(3):035017, 2018.

[66] Samuel Brem, Christopher Linderälv, Paul Erhart, and Ermin Malic. Tunable phases of moiré excitons in van der waals heterostructures. *Nano letters*, 20(12):8534–8540, 2020.

[67] H. Haug and S. W. Koch. *Quantum Theory of the Optical and Electronic Properties of Semiconductors: Fifth Edition*. World Scientific Publishing Company, 2009.

[68] Gunnar Berghäuser and Ermin Malic. Analytical approach to excitonic properties of MoS_2. *Phys. Rev. B*, 89(12):125309, 2014.

[69] Malte Selig, Gunnar Berghäuser, Archana Raja, Philipp Nagler, Christian Schüller, Tony F. Heinz, Tobias Korn, Alexey Chernikov, Ermin Malic, and Andreas Knorr. Excitonic linewidth and coherence lifetime in monolayer transition metal dichalcogenides. *Nat. Commun.*, 7(1):13279, Nov 2016.

[70] Andor Kormányos, Guido Burkard, Martin Gmitra, Jaroslav Fabian, Viktor Zólyomi, Neil D Drummond, and Vladimir Fal'ko. k·p theory for two-dimensional transition metal dichalcogenide semiconductors. *2D Mater.*, 2(2):022001, apr 2015.

[71] Samuel Brem, August Ekman, Dominik Christiansen, Florian Katsch, Malte Selig, Cedric Robert, Xavier Marie, Bernhard Urbaszek, Andreas Knorr, and Ermin Malic. Phonon-assisted photoluminescence from indirect excitons in monolayers of transition-metal dichalcogenides. *Nano Lett.*, 20(4):2849–2856, Apr 2020.

[72] Crispin W Gardiner and Matthew J Collett. Input and output in damped quantum systems: Quantum stochastic differential equations and the master equation. *Phys. Rev. A*, 31(6):3761, 1985.

[73] RS Knox. Theory of excitons. *Solid State Physics, ed. F. Seitz and D. Turnbull (Academic, New York, 1963)*, 1963.

[74] Monique Combescot and Shiue-Yuan Shiau. *Excitons and Cooper pairs: two composite bosons in many-body physics*. Oxford University Press, 2015.

[75] Keliang He, Nardeep Kumar, Liang Zhao, Zefang Wang, Kin Fai Mak, Hui Zhao, and Jie Shan. Tightly bound excitons in monolayer WSe_2. *Phys. Rev. Lett.*, 113(2):026803, 2014.

[76] Miguel M Ugeda, Aaron J Bradley, Su-Fei Shi, H Felipe, Yi Zhang, Diana Y Qiu, Wei Ruan, Sung-Kwan Mo, Zahid Hussain, Zhi-Xun Shen, Feng Wang, Steven G. Louie, and Michael F. Crommie. Giant bandgap renormalization and excitonic effects in a monolayer transition metal dichalcogenide semiconductor. *Nat. Mat.*, 13(12):1091–1095, 2014.

[77] Gang Wang, Alexey Chernikov, Mikhail M. Glazov, Tony F. Heinz, Xavier Marie, Thierry Amand, and Bernhard Urbaszek. Colloquium: Excitons in atomically thin transition metal dichalcogenides. *Rev. Mod. Phys.*, 90:1–2, Apr 2018.

[78] Matthew N Brunetti, Oleg L Berman, and Roman Ya Kezerashvili. Optical absorption by indirect excitons in a transition metal dichalcogenide/hexagonal boron nitride heterostructure. *J. Phys. Condens. Matter*, 30(22):225001, 2018.

[79] Florian Katsch, Malte Selig, Alexander Carmele, and Andreas Knorr. Theory of exciton–exciton interactions in monolayer transition metal dichalcogenides. *Phys. Status Solidi B*, 255(12):1800185, 2018.

[80] AL Ivanov and H Haug. Self-consistent theory of the biexciton optical nonlinearity. *Phys. Rev. B*, 48(3):1490, 1993.

[81] Yutaka Toyozawa. Theory of line-shapes of the exciton absorption bands. *Progress of Theoretical Physics*, 20(1):53–81, 1958.

[82] S. Brem, M. Selig, G. Berghaeuser, and E. Malic. Exciton relaxation cascade in two-dimensional transition metal dichalcogenides. *Sci. Rep.*, 8:8238, 2018.

[83] Zhenghe Jin, Xiaodong Li, Jeffrey T. Mullen, and Ki Wook Kim. Intrinsic transport properties of electrons and holes in monolayer transition-metal dichalcogenides. *Phys. Rev. B*, 90:045422, Jul 2014.

[84] Roberto Rosati, Koloman Wagner, Samuel Brem, Raül Perea-Causín, Edith Wietek, Jonas Zipfel, Jonas D. Ziegler, Malte Selig, Takashi Taniguchi, Kenji Watanabe, Andreas Knorr, Alexey Chernikov, and

Ermin Malic. Temporal evolution of low-temperature phonon sidebands in transition metal dichalcogenides. *ACS Photonics*, 7(10):2756–2764, Oct 2020.

[85] Galan Moody, Chandriker Kavir Dass, Kai Hao, Chang-Hsiao Chen, Lain-Jong Li, Akshay Singh, Kha Tran, Genevieve Clark, Xiaodong Xu, Gunnar Berghäuser, et al. Intrinsic homogeneous linewidth and broadening mechanisms of excitons in monolayer transition metal dichalcogenides. *Nat. Commun.*, 6(1):1–6, 2015.

[86] Maciej R Molas, Clement Faugeras, Autur O Slobodeniuk, Karol Nogajewski, Miroslav Bartos, DM Basko, and Marek Potemski. Brightening of dark excitons in monolayers of semiconducting transition metal dichalcogenides. *2D Materials*, 4(2):021003, 2017.

[87] You Zhou, Giovanni Scuri, Dominik S Wild, Alexander A High, Alan Dibos, Luis A Jauregui, Chi Shu, Kristiaan De Greve, Kateryna Pistunova, Andrew Y Joe, et al. Probing dark excitons in atomically thin semiconductors via near-field coupling to surface plasmon polaritons. *Nature nanotechnology*, 12(9):856–860, 2017.

[88] Galina Khitrova, HM Gibbs, M Kira, Stephan W Koch, and Axel Scherer. Vacuum Rabi splitting in semiconductors. *Nat. Phys.*, 2(2):81–90, 2006.

[89] Denis G Baranov, Martin Wersall, Jorge Cuadra, Tomasz J Antosiewicz, and Timur Shegai. Novel nanostructures and materials for strong light–matter interactions. *Acs Photonics*, 5(1):24–42, 2018.

[90] Fengrui Hu and Zhe Fei. Recent progress on exciton–polaritons in layered transition-metal dichalcogenides. *Adv. Opt. Mater.*, 8(5):1901003, 2020.

[91] F. Lengers, T. Kuhn, and D. E. Reiter. Phonon signatures in spectra of exciton polaritons in transition metal dichalcogenides. *Phys. Rev. B*, 104:L241301, Dec 2021.

[92] F. Cadiz, E. Courtade, C. Robert, G. Wang, Y. Shen, H. Cai, T. Taniguchi, K. Watanabe, H. Carrere, D. Lagarde, M. Manca,

T. Amand, P. Renucci, S. Tongay, X. Marie, and B. Urbaszek. Excitonic linewidth approaching the homogeneous limit in MoS_2-based van der Waals heterostructures. *Phys. Rev. X*, 7:021026, May 2017.

[93] Dominik Christiansen, Malte Selig, Gunnar Berghäuser, Robert Schmidt, Iris Niehues, Robert Schneider, Ashish Arora, Steffen Michaelis de Vasconcellos, Rudolf Bratschitsch, Ermin Malic, and Andreas Knorr. Phonon sidebands in monolayer transition metal dichalcogenides. *Phys. Rev. Lett.*, 119:187402, Nov 2017.

[94] Aymeric Delteil, Thomas Fink, Anne Schade, Sven Höfling, Christian Schneider, and Ataç İmamoğlu. Towards polariton blockade of confined exciton–polaritons. *Nat. Mat.*, 18(3):219–222, 2019.

[95] A Thränhardt, S Kuckenburg, A Knorr, T Meier, and SW Koch. Quantum theory of phonon-assisted exciton formation and luminescence in semiconductor quantum wells. *Phys, Rev. B*, 62(4):2706, 2000.

[96] Fausto Rossi. *Theory of semiconductor quantum devices: microscopic modeling and simulation strategies*. Springer Science & Business Media, 2011.

[97] J. Schilp, T. Kuhn, and G. Mahler. Electron-phonon quantum kinetics in pulse-excited semiconductors: Memory and renormalization effects. *Phys. Rev. B*, 50:5435–5447, Aug 1994.

[98] F. Lengers, T. Kuhn, and D. E. Reiter. Theory of the absorption line shape in monolayers of transition metal dichalcogenides. *Phys. Rev. B*, 101:155304, Apr 2020.

[99] Samuel Brem, Jonas Zipfel, Malte Selig, Archana Raja, Lutz Waldecker, Jonas D Ziegler, Takashi Taniguchi, Kenji Watanabe, Alexey Chernikov, and Ermin Malic. Intrinsic lifetime of higher excitonic states in tungsten diselenide monolayers. *Nanoscale*, 11(25):12381–12387, 2019.

[100] Nardeep Kumar, Qiannan Cui, Frank Ceballos, Dawei He, Yongsheng Wang, and Hui Zhao. Exciton diffusion in monolayer and bulk $MoSe_2$. *Nanoscale*, 6(9):4915–4919, 2014.

[101] L. Yuan, T. Wang, T. Zhu, M. Zhou, and L. Huang. Exciton dynamics, transport, and annihilation in atomically thin two-dimensional semiconductors. *J. Phys. Chem. Lett.*, 8:3371, 2017.

[102] Toshiaki Kato and Toshiro Kaneko. Transport dynamics of neutral excitons and trions in monolayer WS_2. *ACS Nano*, 10(10):9687–9694, Oct 2016.

[103] F. Cadiz, C. Robert, E. Courtade, M. Manca, L. Martinelli, T. Taniguchi, K. Watanabe, T. Amand, A. C. H. Rowe, D. Paget, B. Urbaszek, and X. Marie. Exciton diffusion in WSe_2 monolayers embedded in a Van der Waals heterostructure. *Appl. Phys. Lett.*, 112(15):152106, 2018.

[104] Ortwin Hess and Tilmann Kuhn. Maxwell-Bloch equations for spatially inhomogeneous semiconductor lasers: I. theoretical formulation. *Phys. Rev. A*, 54:3347–3359, Oct 1996.

[105] Jonas Zipfel, Marvin Kulig, Raül Perea-Causín, Samuel Brem, Jonas D Ziegler, Roberto Rosati, Takashi Taniguchi, Kenji Watanabe, Mikhail M Glazov, Ermin Malic, et al. Exciton diffusion in monolayer semiconductors with suppressed disorder. *Phys. Rev. B*, 101(11):115430, 2020.

[106] Shudi Pan, Weijin Kong, Jianhua Liu, Xiaohui Ge, Peymon Zereshki, Shengcai Hao, Dawei He, Yongsheng Wang, and Hui Zhao. Understanding spatiotemporal photocarrier dynamics in monolayer and bulk $MoTe_2$ for optimized optoelectronic devices. *Appl. Nano Mater.*, 2(1):459–464, 2018.

[107] Viktar S Asadchy, Mohammad Sajjad Mirmoosa, Ana Diaz-Rubio, Shanhui Fan, and Sergei A Tretyakov. Tutorial on electromagnetic nonreciprocity and its origins. *Proc. IEEE*, 108(10):1684–1727, 2020.

[108] Richard B Adler, Lan Jen Chu, and Robert M Fano. *Electromagnetic energy transmission and radiation.* Wiley, 1960.

[109] Hermann Haus. *Waves and fields in optoelectronics.* Prentice-Hall, 1984.

[110] LC Botten, RC McPhedran, NA Nicorovici, and GH Derrick. Periodic models for thin optimal absorbers of electromagnetic radiation. *Phys. Rev. B*, 55(24):R16072, 1997.

[111] Jessica R Piper, Victor Liu, and Shanhui Fan. Total absorption by degenerate critical coupling. *Appl. Phys. Lett.*, 104(25):251110, 2014.

[112] Y Chen, A Tredicucci, and F Bassani. Bulk exciton polaritons in GaAs microcavities. *Phys. Rev. B*, 52(3):1800, 1995.

[113] Stanley Pau, Gunnar Björk, Joseph Jacobson, Hui Cao, and Yoshihisa Yamamoto. Microcavity exciton-polariton splitting in the linear regime. *Phys. Rev. B*, 51(20):14437, 1995.

[114] Hangyong Shan, Ivan Iorsh, Bo Han, Christoph Rupprecht, Heiko Knopf, Falk Eilenberger, Martin Esmann, Kentaro Yumigeta, Kenji Watanabe, Takashi Taniguchi, et al. Brightening of a dark monolayer semiconductor via strong light-matter coupling in a cavity. *Nature Comm.*, 13(1):1–7, 2022.